

# Measurement of the muon beam direction and muon flux for the T2K neutrino experiment

K. Suzuki<sup>1,\*</sup>, S. Aoki<sup>2</sup>, A. Ariga<sup>3</sup>, T. Ariga<sup>3</sup>, F. Bay<sup>3,†</sup>, C. Bronner<sup>4</sup>, A. Ereditato<sup>3</sup>, M. Friend<sup>5</sup>, M. Hartz<sup>4,8</sup>, T. Hiraki<sup>1</sup>, A.K. Ichikawa<sup>1</sup>, T. Ishida<sup>5</sup>, T. Ishii<sup>5</sup>, F. Juget<sup>3,‡</sup>, T. Kikawa<sup>1,§</sup>, T. Kobayashi<sup>5</sup>, H. Kubo<sup>1</sup>, K. Matsuoka<sup>1,¶</sup>, T. Maruyama<sup>5</sup>, A. Minamino<sup>1</sup>, A. Murakami<sup>1,||</sup>, T. Nakadaira<sup>5</sup>, T. Nakaya<sup>1</sup>, K. Nakayoshi<sup>5</sup>, Y. Oyama<sup>5</sup>, C. Pistillo<sup>3</sup>, K. Sakashita<sup>5</sup>, T. Sekiguchi<sup>5</sup>, S.Y. Suzuki<sup>5</sup>, S. Tada<sup>5</sup>, Y. Yamada<sup>5</sup>, K. Yamamoto<sup>6</sup>, and M. Yokoyama<sup>7</sup>

<sup>1</sup>*Department of Physics, Kyoto University, Kyoto, Japan*

<sup>2</sup>*Kobe University, Kobe, Japan*

<sup>3</sup>*University of Bern, Albert Einstein Center for Fundamental Physics, Laboratory for High Energy Physics (LHEP), Bern, Switzerland*

<sup>4</sup>*Kauli Institute for the Physics and Mathematics of the Universe (WPI), Todai Institutes for Advanced Study, University of Tokyo, Kashiwa, Japan*

<sup>5</sup>*High Energy Accelerator Research Organization (KEK), Tsukuba, Ibaraki, Japan*

<sup>6</sup>*Department of Physics, Osaka City University, Osaka, Japan*

<sup>7</sup>*Department of Physics, University of Tokyo, Tokyo, Japan*

<sup>8</sup>*TRIUMF, Vancouver, British Columbia, Canada*

\**E-mail: k.suzuki@scphys.kyoto-u.ac.jp*

.....  
 The Tokai-to-Kamioka (T2K) neutrino experiment measures neutrino oscillations by using an almost pure muon neutrino beam produced at the J-PARC accelerator facility. The T2K muon monitor was installed to measure the direction and stability of the muon beam which is produced together with the muon neutrino beam. The systematic error in the muon beam direction measurement was estimated, using data and MC simulation, to be 0.28 mrad. During beam operation, the proton beam has been controlled using measurements from the muon monitor and the direction of the neutrino beam has been tuned to within 0.3 mrad with respect to the designed beam-axis. In order to understand the muon beam properties, measurement of the absolute muon yield at the muon monitor was conducted with an emulsion detector. The number of muon tracks was measured to be  $(4.06 \pm 0.05) \times 10^4 \text{ cm}^{-2}$  normalized with  $4 \times 10^{11}$  protons on target with 250 kA horn operation. The result is in agreement with the prediction which is corrected based on hadron production data.

---

<sup>†</sup> Present address: Institute for Particle Physics, ETH Zurich, Zurich, Switzerland

<sup>‡</sup> Present address: Institute of Radiation Physics, University Hospital and University of Lausanne, Lausanne, Switzerland

<sup>§</sup> Present address: RCNP, Osaka University, Ibaraki, Osaka, Japan

<sup>¶</sup> Present address: KMI, Nagoya University, Nagoya, Japan

<sup>||</sup> Present address: Toshiba Corporation, Kawasaki, Japan

## 1. Introduction

The Tokai-to-Kamioka (T2K) experiment [1] is a long baseline neutrino oscillation experiment in Japan. The neutrino oscillation parameters are determined by measuring an accelerator-produced neutrino beam before oscillation with the near detector and near the oscillation maximum with the far detector. T2K began operation in January 2010. Since then, data corresponding to a total of  $6.63 \times 10^{20}$  protons on target (p.o.t.) had been collected up to May 2013.

The T2K muon monitor [2] was installed to monitor the muon beam which is produced together with the neutrino beam from the decay of pions. As the muon monitor is the only detector to monitor the beam spill-by-spill, our strategy is to monitor the muon beam direction with a precision of 0.3 mrad for every beam spill, in order to better control the neutrino beam for the neutrino oscillation measurement.

In this paper, we first provide an overview of the T2K experiment and the importance of a precise measurement of the muon beam direction in Sec. 2. Section 3 gives an overview of the components of the muon monitor. A method for reconstructing the profile of the muon beam with the muon monitor is described in Sec. 4. In this section we also show the systematic error in the beam direction measurement, which was estimated using both the actual beam data and MC simulation. The stability of the beam direction and its intensity during the T2K beam operation is discussed in Sec. 5. During the beam operation, measurements of the absolute muon yield were conducted using an emulsion detector. This result, and a comparison with the MC prediction, are shown in Secs. 6 and 7 respectively.

## 2. Overview of the T2K experiment

T2K consists of: a neutrino beamline, producing an intense muon neutrino beam; a near detector complex, INGRID and ND280; and a far detector, Super-Kamiokande (Super-K). Using this setup, the experiment aims to measure the neutrino oscillation parameters. An overview of the T2K experiment is shown in Fig. 1. The Japan Proton Accelerator Research Complex (J-PARC) is a facility situated in Tokai, Japan. A proton beam is accelerated up to 30 GeV by the main ring synchrotron and is fast-extracted to the neutrino beamline. The neutrino beamline consists of two components as shown in Fig. 2: a primary and secondary beamline. In the primary beamline, the proton beam is transported to a graphite target every 2 to 3 seconds. The beam has a time structure of eight narrow bunches, 58 ns long with 581 ns intervals, in a single spill. The beam forms a two dimensional Gaussian distribution of  $\sim 4$  mm  $1\sigma$  width corresponding to  $\sim 7$  mm radius at the target. The target and other equipment used to produce the neutrino beam is situated in the secondary beam line, whose details are given in Sec. 2.1. The neutrino beam produced here is detected at ND280 and Super-K, and the oscillation parameters are then measured.

### 2.1. Creation of the neutrino beam at the secondary beamline

Figure 3 provides an overview of the secondary beamline. All of the components in the beamline are contained in a single volume of  $\sim 1500$  m<sup>3</sup> filled with helium gas, which is enclosed by a helium vessel. The proton beam, transported to the target via the primary beamline, first enters a baffle which works as a collimator. After passing through the baffle,

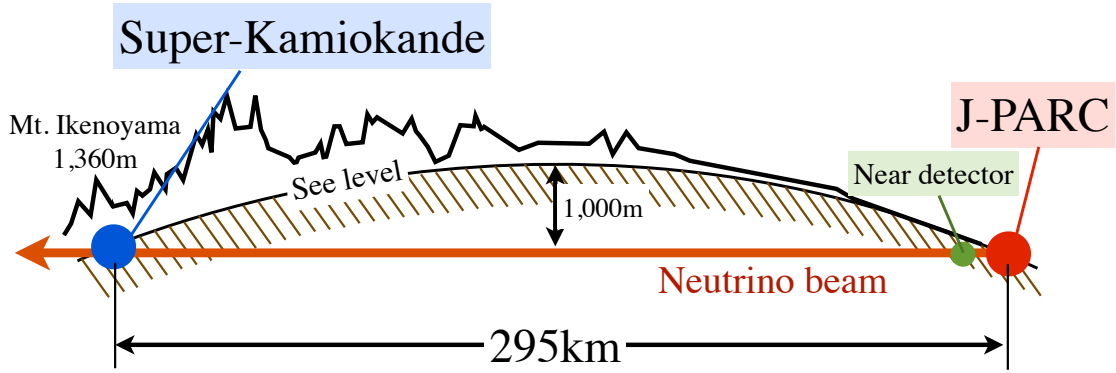


Fig. 1: Overview of the T2K experiment.

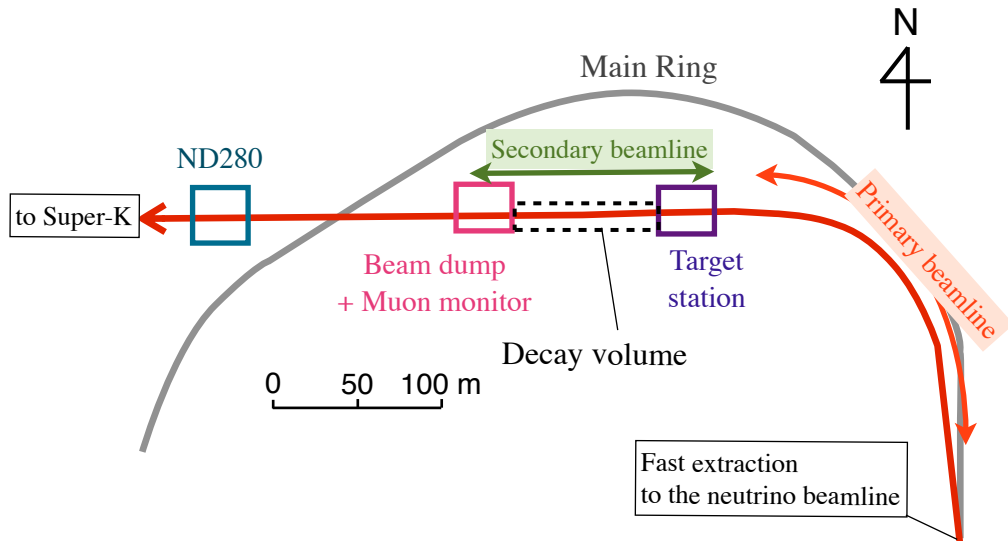


Fig. 2: Overview of the T2K beamline.

the proton beam hits the target and produces secondary particles, mostly pions. Three magnetic horns [3] are used to focus (defocus) these positively (negatively) charged pions along the designed beam-axis. Each of the horns is made of aluminum conductor and produces a maximum toroidal magnetic field of 1.7 T inside the conductor when the horns operate at 250 kA. The decay volume for the pions is a 96 m long steel tunnel. A pure and intense muon neutrino beam is produced as the pions decay in this tunnel. The beam dump sits at the end of the decay volume to absorb the hadron flux from the beam. It consists of a core composed of 75 tons of graphite and fifteen (two) iron plates placed outside (inside) the helium vessel at the downstream end of the core. The length is 3.174 m, in line with the beam-axis.

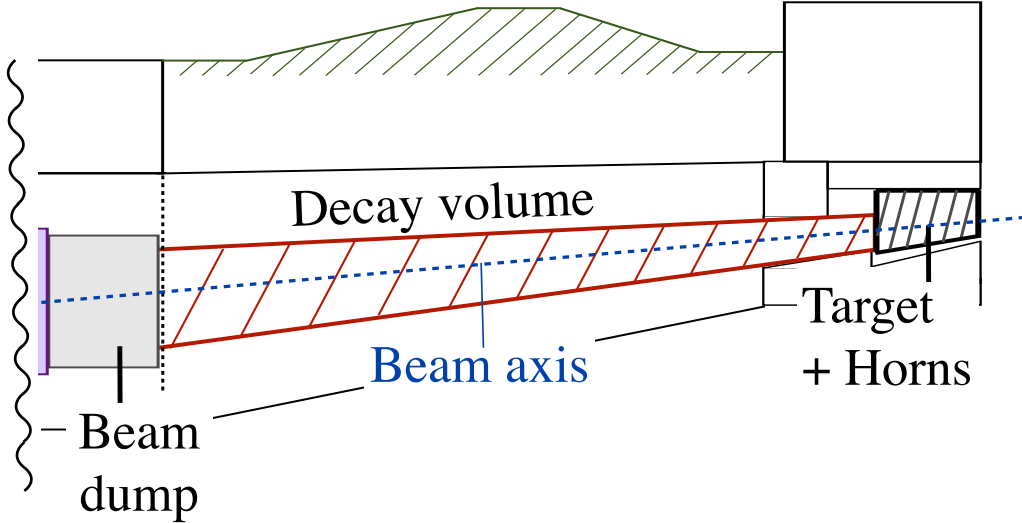


Fig. 3: Overview of the secondary beamline. All of the components in the beamline, the target, horns, decay volume and beam dump, are contained in a single volume of  $1500 \text{ m}^3$  filled with helium gas.

### 2.2. Importance of measuring the neutrino beam direction and intensity

Both ND280 and Super-K are located  $2.5$  degrees from the beam-axis. This experimental setup enables us to utilize a narrow-band neutrino beam with a peak energy around  $0.6 \text{ GeV}$  at which neutrinos oscillate with near the maximum probability after traveling  $295 \text{ km}$ . However, a  $1 \text{ mrad}$  uncertainty in the beam direction measurement leads to a  $2\text{-}3 \%$  uncertainty in the neutrino energy scale, affecting measurements of the neutrino oscillation parameters. Therefore the beam direction has to be monitored with a good precision and controlled well to eliminate the additional uncertainty for the oscillation parameters. In addition, a contingency may arise in the beamline during operation, such as a sudden drop in the horn currents or deterioration of the target, resulting in a decrease in the neutrino beam intensity. Therefore, monitoring not only the direction but also the intensity of the neutrino beam has to be done on a spill-by-spill basis in order to promptly confirm the state and health of the beamline components as well as quality of the neutrino beam.

### 2.3. Beam monitors

T2K employs two beam monitors for the beam direction measurement, INGRID and the muon monitor. INGRID [4] is located  $280 \text{ m}$  downstream of the target. It has  $14$  independent modules which are composed of sandwiched iron plates and scintillator planes. The modules are installed at positions in cross shape centered on the beam-axis. The profile of the neutrino beam is reconstructed by counting the number of neutrino interactions in each of the modules. Due to the small cross section of the neutrino interactions, the time for accumulating neutrino events depends on the beam intensity and typically requires one day for the profile reconstruction with a proton beam power of  $\sim 100 \text{ kW}$ .

The T2K muon monitor is another beam monitor that monitors the muon beam which is produced together with the neutrino beam from the decay of pions. The monitor is located

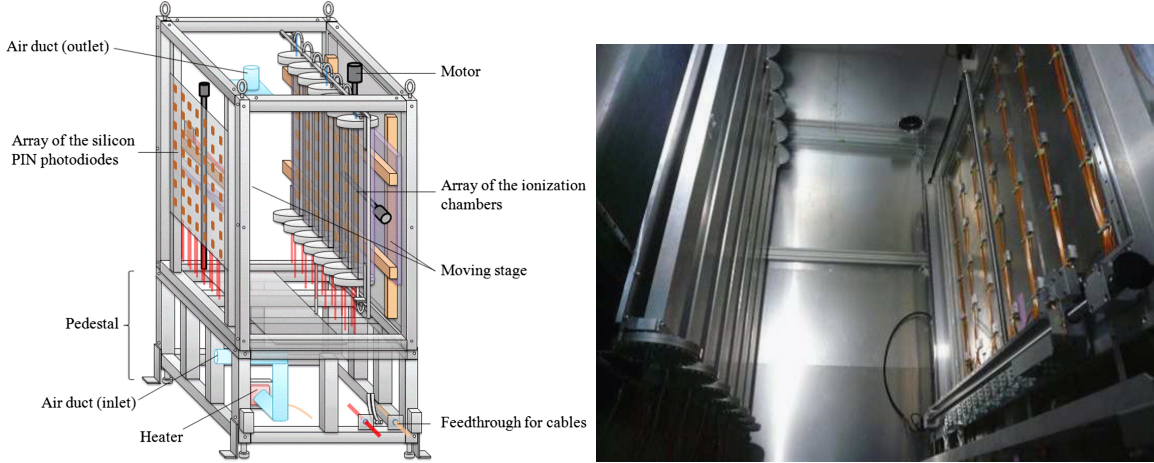


Fig. 4: Schematic view (left) and the photograph of the muon monitor (right). The monitor consists of array of the ionization chamber and the silicon PIN photodiode. The muon beam enters into the array of the silicon PIN photodiodes first and then goes through the array of the ionization chamber [2].

118 m downstream of the target and just downstream of the beam dump which absorbs the hadron flux. Unlike the INGRID measurement, the muon monitor can detect the muon beam spill-by-spill. Therefore, the intensity and direction of neutrino beam can be indirectly monitored with the muon monitor spill-by-spill. It is necessary to monitor the muon beam direction with a precision of 0.3 mrad in order to control the neutrino beam direction to within 0.3 mrad with respect to the beam-axis.

### 3. Instrumentation of the muon monitor

The T2K muon monitor was installed in the muon pit located just downstream of the beam dump and 18.5 m underground. Details of the design of the monitor are described in [2]. The thickness of the beam dump is chosen to minimize the hadron flux while retaining the sensitivity in the measurement of the muon beam direction; only muons with energy above 5 GeV can pass through the beam dump and reach the muon monitor. Figure 4 shows a schematic view (left) and photograph (right) of the muon monitor. The monitor consists of two independent detectors: an array of ionization chambers and another array of silicon PIN photodiodes. Each detector array has  $7 \times 7 = 49$  sensors at 25 cm intervals and covers an area of  $150 \times 150 \text{ cm}^2$  with respect to the beam-axis.

#### 3.1. Ionization chamber

Each of the seven ionization chambers contains seven sets of two parallel  $100 \times 100 \text{ mm}^2$  ceramic plates separated by 3 mm. One of the two parallel plates has a signal electrode which has a dimension of  $75 \times 75 \text{ mm}^2$  and is surrounded by the ground electrodes. A bias voltage of 200 V is applied to a  $93 \times 93 \text{ mm}^2$  electrode on the other plate and a uniform electric field is created through a  $75 \times 75 \text{ mm}^2$  area between the two electrodes. Thus, ionization pairs generated only in the  $75 \times 75 \times 3 \text{ mm}^3$  volume contribute to the signal. All of the chambers are filled with a gas mixture set to be 98% Ar and 2% N<sub>2</sub> for a beam intensity below  $2.3 \times 10^{13}$  protons per bunch (p.p.b.). For higher beam intensity, 99% He and 1% N<sub>2</sub>

is used instead as the size of the signal with He gas is  $\sim 10$  times smaller than that with Ar gas. In both of the gas systems,  $N_2$  is used as a quencher and to render the signal insensitive to the amount of impurities in the gas via the Jesse effect [5].

### 3.2. Silicon PIN photodiode

The silicon PIN photodiode (HAMAMATSU<sup>®</sup> S3590-08) has an active area of  $10 \times 10 \text{ mm}^2$  and a depletion layer thickness of  $300 \text{ }\mu\text{m}$ . The silicon layer is mounted on a ceramic base. In order to fully deplete the layer, a bias voltage of  $80 \text{ V}$  is applied. The photodiode is put on a PEEK<sup>™</sup> base fixed to the support enclosure and is covered by an aluminum base.

The silicon PIN photodiode is not tolerant of the severe radiation in the muon pit. There is a report [6] that the depletion voltage of the silicon PIN detector falls 50% at about  $0.7 \times 10^{13} \text{ protons/cm}^2$  and reaches a minimum at  $1.25 \times 10^{13} \text{ protons/cm}^2$ . The decrease in the signal was also reported in the beam test where a  $100 \text{ MeV}$  electron beam was used [2]. From these results, it was estimated that the signal starts to decrease after a one month exposure to the muon beam in the case of  $0.75 \text{ MW}$  beam operation.

### 3.3. Electronics

Both signals from the ionization chamber and silicon PIN photodiodes are transmitted by about  $70 \text{ m}$  of co-axial cables which connect the muon pit underground to an electronics hut on the surface. The signals are digitized by Flash-ADC modules (FADC) of the COPPER system [7] developed by KEK. The resolution and sampling rate of the FADC are 12 bit and  $65 \text{ MHz}$ , respectively. For the signal from the ionization chamber, the gain in the FADC is set to 5. On the other hand, unity gain is set for the signal from the photodiodes since the size of the signal is about 30 times larger than that of the signal from the ionization chambers. Instead, the signal from the photodiode is attenuated by 0, 15, and 30 dB depending on the beam intensity. Both FADC and signal cable are well calibrated with a CAMAC charge/time generator (Phillips 7120) with 1% precision.

## 4. Measurement of the muon beam direction

The signal from each of the sensors are read out by the FADC and integrated to calculate the collected charge. The profile of the muon beam is then reconstructed by fitting the two-dimensional charge distribution with a two-dimensional Gaussian function. Details of the analysis method are described in Sec. 4.1. We also prepare MC simulation for the prediction of the muon flux: simulation of hadronic interactions inside and outside of the target and calculation of the particle decay in the decay volume. Section 4.2 explains the simulation in more detail. The sensors are calibrated using the actual beam at the beginning of each beam operation period as described in Sec. 4.3. The systematic error for the beam direction measurement was estimated using both the actual beam data and MC simulation, this is detailed in Sec. 4.4.

### 4.1. Reconstruction of the muon beam profile

The collected charge is calculated for each sensor by integrating a waveform digitized by the FADC. The typical waveforms recorded during beam operation are shown in Fig. 5. These waveforms were obtained at a beam intensity of  $1.3 \times 10^{13} \text{ p.p.b.}$  where the attenuator level

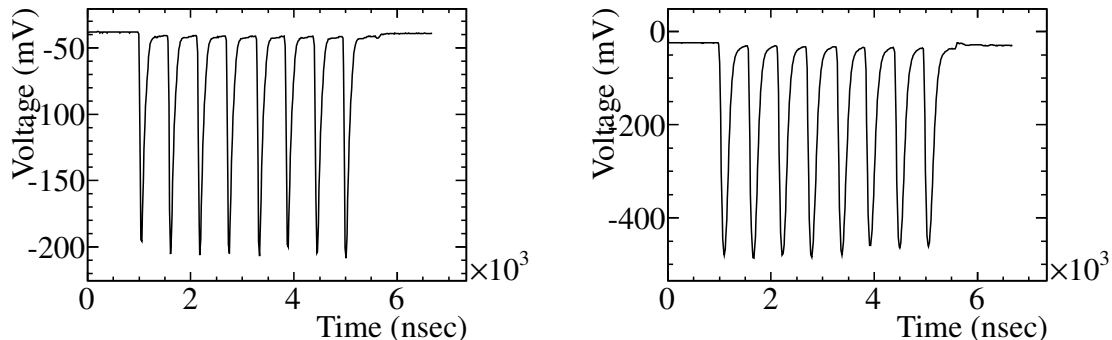


Fig. 5: Waveform of the signal from the silicon PIN photodiode (left) and ionization chamber (right), digitized by the FADC. Both of the signals are from sensors placed at the center of the arrays and recorded when the beam intensity is  $1.3 \times 10^{13}$  p.p.b. The attenuator level was set to 30 dB for the signal from the silicon sensors.

was set to 30 dB for the signal from the silicon sensors. In the analysis, the integration windows are set to each bunch so that the profile of the muon beam can be reconstructed bunch-by-bunch. Once the collected charge is calculated for each bunch, it is then summed over all bunches to get the muon beam direction and intensity. In this way, the measurement precision statistically improved by the square root of the number of bunches. A left in Fig. 6 shows the charged distribution measured by the silicon PIN photodiodes, which is obtained by summing the distribution over all bunches. In order to extract the profile of the muon beam, the distribution is then fitted by a two-dimensional Gaussian function defined as follows:

$$f(x, y) = A \exp \left[ -\frac{(x - x_0)^2}{2\sigma_x^2} - \frac{(y - y_0)^2}{2\sigma_y^2} \right] \quad (1)$$

where  $A$  is a normalization parameter;  $x_0$  and  $y_0$  represent centers of the beam profile in the horizontal and vertical direction, respectively;  $\sigma_x$  and  $\sigma_y$  represent widths of the beam profile in the horizontal and vertical direction, respectively. An example of the reconstructed profile obtained from a fit of the two-dimensional Gaussian is shown on the right in Fig. 6. Figure 7 shows profiles of the muon beam for the horn currents of 0 kA and 250 kA. The peak charge collected at 250 kA operation is about 4 times larger than that collected at 0 kA operation. The muon beam direction  $\{\theta_x, \theta_y\}$  is then calculated using parameters  $\{x_0, y_0\}$  and distance ( $= L$ ) between the target and muon monitor:

$$\theta_x = x_0/L, \quad \theta_y = y_0/L \quad (L = 118 \text{ m}) \quad (2)$$

Here we use an approximation of  $\tan \theta_{x(y)} \simeq \theta_{x(y)}$ , as  $\theta_{x(y)} \ll 1$ .

#### 4.2. Monte Carlo simulation

The MC simulation consists of two processes: a simulation of the hadronic interaction in the graphite target, and propagation of the secondary particles until they interact or decay. The hadronic interaction in the target is simulated with FLUKA2008 [8] which was found

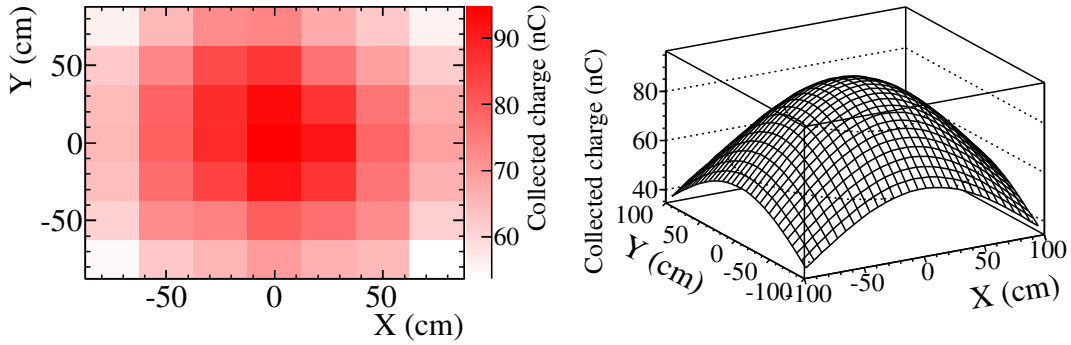


Fig. 6: Charge distribution (left) and reconstructed profile (right) of the muon beam measured by the silicon array. The collected charge is obtained for each sensor by integrating the waveform of all of the bunches (i.e spill) read out by the FADC. This is a beam event when the intensity is  $1.3 \times 10^{13}$  p.p.b.

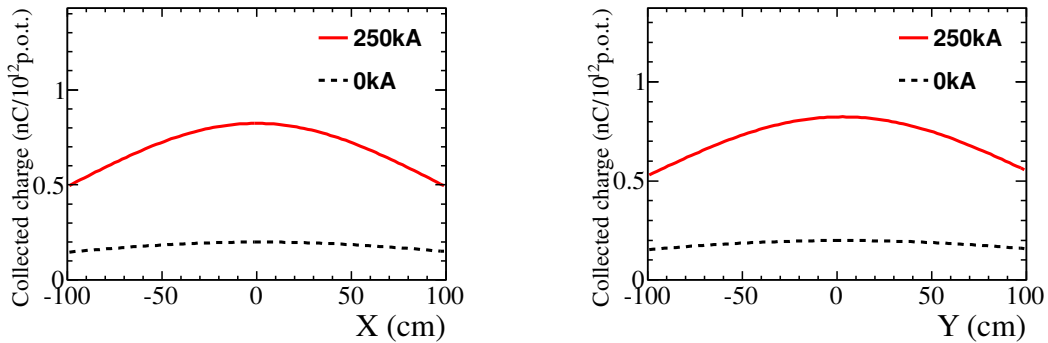


Fig. 7: Muon beam profile obtained with the silicon array when horns are operated at 0 kA (dashed black) and 250 kA (solid red). The horizontal (vertical) profile is shown in left (right).

to be in better agreement with external hadron production data <sup>1,2</sup>. Kinematic information for particles emitted from the target is saved and transferred to the JNUBEAM simulation [9]. JNUBEAM is a GEANT3 [10] simulation of the secondary beamline including the muon monitor. The geometry of these components is modeled based on the final mechanical drawings of the constructed beamline. Hadronic interactions are modeled by GCALOR [11] in JNUBEAM. Table 1 shows the MC estimation of flux of particles penetrating the muon monitor at the 250 kA horn current setting. The muon are accompanied by soft components such as gammas and  $\delta$ -ray electrons. The particles contributing to the signal at the muon

<sup>1</sup> Recently FLUKA2011 is found to be the best agreement with external hadron production data.

<sup>2</sup> The hadron interactions are further tuned with the external experiment data in Sec. 7.



Table 1: Breakdown of the particles ( $/10^{13}$  p.o.t.) arriving at the muon pit and going through the area covered by the muon monitor ( $150 \times 150$  cm<sup>2</sup>). These are estimated by the MC simulation with 250 kA horn current settings.

Particle type	Particles at the silicon array		Particles at the chamber array	
$\mu^+$	$2.39 \times 10^{10}$	(49.3%)	$2.20 \times 10^{10}$	(52.0%)
$\mu^-$	$0.18 \times 10^{10}$	(3.7%)	$0.17 \times 10^{10}$	(3.9%)
$e^-$	$0.32 \times 10^{10}$	(6.7%)	$0.26 \times 10^{10}$	(6.3%)
$e^+$	$0.03 \times 10^{10}$	(0.6%)	$0.02 \times 10^{10}$	(0.6%)
$\gamma$	$1.92 \times 10^{10}$	(39.6%)	$1.56 \times 10^{10}$	(37.0%)
others	$< 0.01 \times 10^{10}$	(0.1%)	$< 0.01 \times 10^{10}$	(0.2%)
Total	$4.84 \times 10^{10}$	(100%)	$4.22 \times 10^{10}$	(100%)

Table 2: Breakdown of the particles ( $/10^{13}$  p.o.t.) contributing to the signal at the muon monitor. The number listed in the table is estimated for particles going through the area covered by the monitor ( $150 \times 150$  cm<sup>2</sup>). In this MC estimation, argon gas is used for the ionization chamber and horn currents are set to 250 kA.

Particle type	Particles at the silicon array		Particles at the chamber array	
$\mu^+$	$2.39 \times 10^{10}$	(82.2%)	$2.19 \times 10^{10}$	(83.4%)
$\mu^-$	$0.18 \times 10^{10}$	(6.1%)	$0.17 \times 10^{10}$	(6.3%)
$e^-$	$0.30 \times 10^{10}$	(10.2%)	$0.25 \times 10^{10}$	(9.3%)
$e^+$	$0.03 \times 10^{10}$	(0.9%)	$0.02 \times 10^{10}$	(0.9%)
$\gamma$ and others	$0.02 \times 10^{10}$	(0.6%)	$< 0.01 \times 10^{10}$	(<0.1%)
Total	$2.90 \times 10^{10}$	(100%)	$2.63 \times 10^{10}$	(100%)

monitor is also estimated using the MC simulation where argon gas is used for the ionization chamber and horn currents are set to 250 kA. The result is shown in Table 2. In both the silicon and ionization chamber arrays, the muons account for about 80% of the total amount of the signal. The subsequent contribution to the signal comes from  $\delta$ -ray, accounting for about 10% of the total. A breakdown of the muon flux by the parent particles ( $\pi^\pm$ ,  $K^\pm$  and  $K_L^0$ ) is shown in Table 3. As listed in the table, 92% (95%) of total  $\mu^+$  ( $\mu^-$ ) production is attributable to parent  $\pi^+$  ( $\pi^-$ ). Table 4 shows the breakdown of parent particles ( $\pi^\pm$  and  $K^\pm$ ) generated at each of the materials in the secondary beamline. Most of the pions contributing to the muon flux are generated at the graphite target. The subsequent contributions from pions come from interactions at the beam dump (carbon) which is placed just in front of the muon monitor.

### 4.3. Detector calibration

Both of the detectors, silicon PIN photodiodes and ionization chambers, are relatively calibrated using the real beam at the beginning of each beam operation period. The ionization

Table 3: Breakdown of the muon flux by the parent particles ( $\pi^\pm$ ,  $K^\pm$  and  $K_L^0$ ) for the 250 kA horn current setting.

Parent particle	$\mu^+$ ( $\mu^-$ )
$\pi^+$ ( $\pi^-$ )	91.73% (94.71%)
$K^+$ ( $K^-$ )	8.26% (5.13%)
$K_L^0$	0.01% (0.16%)

Table 4: Breakdown of the muon parent particles generated at each material for the 250 kA horn setting. The last column shows the breakdown for the total flux. A symbol in a parenthesis denotes the main material element.

Material	$\pi^+$	$\pi^-$	$K^+$	$K^-$	Total
Graphite target (C)	94.00%	64.00%	89.80%	53.94%	91.58%
Horn (Al)	1.52%	3.92%	1.16%	1.02%	1.65%
Decay volume (He)	1.24%	6.70%	0.99%	3.34%	1.59%
Decay volume (Fe)	0.35%	3.94%	0.65%	2.83%	0.61%
Beam dump (C)	2.36%	20.80%	7.15%	38.36%	4.06%
Other materials	0.53%	0.63%	0.25%	0.51%	0.51%
	100%	100%	100%	100%	100%

chamber is calibrated by moving the entire chamber array by  $\pm 25$  cm in both the horizontal and vertical direction and measuring the muon profile at nine different configurations<sup>3</sup>. These nine measured profiles should be the same on the assumption that the muon beam profile itself does not change over the course of the measurements. In this way the 49 sensors are relatively calibrated with a precision of 0.4%.

The silicon PIN photodiodes are calibrated sensor-by-sensor by measuring the muon beam with an extra calibration sensor mounted on small moving stage behind the silicon array (see Fig. 8). The calibration sensor is placed behind each sensor and the collected charge ratio of the moving sensor to each of the other sensors is measured:

$$R_i = Q_i/Q_{ref} \quad (i = 1, 2, \dots, 49) \quad (3)$$

where  $Q_{ref}$  and  $Q_i$  are the collected charges obtained by the extra calibration sensor and  $i^{th}$  signal sensor, respectively. The correction factor is then calculated for each sensor using the mean of the charge ratios:

$$G_i = \langle R \rangle / R_i \quad (4)$$

This correction is then applied to each sensor. In this way, all of the sensors are calibrated with a precision of 0.1%.

#### 4.4. Systematic error in the beam direction measurement

The systematic error in the beam direction comes from:

<sup>3</sup> The 25 cm is equal to the interval of the sensors.

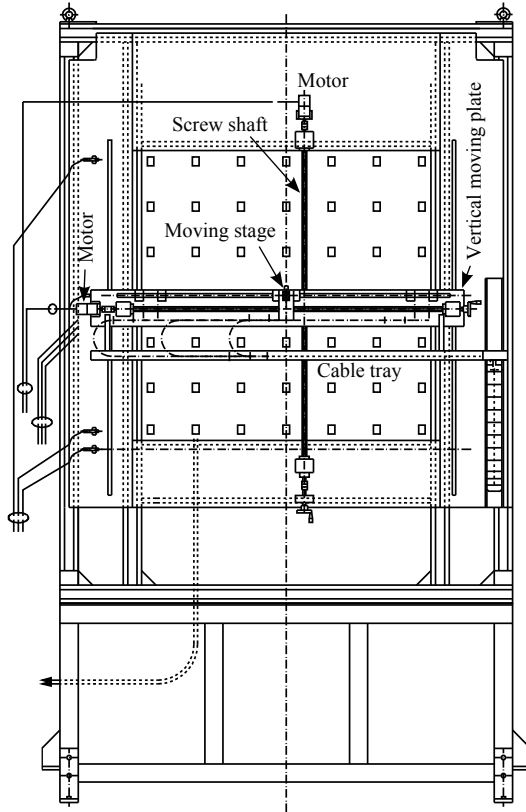


Fig. 8: Moving stage for the calibration silicon PIN photodiode, as viewed from downstream.

- (1) uncertainty of the structure of the upstream materials,
- (2)  $\delta$ -ray contamination in the muon beam,
- (3) uncertainty in the relative calibration of the sensors,
- (4) alignment error of the muon monitor,
- (5) effect from the tilted beamline.

The first three sources cause a distortion in the observed beam profile and lead to an uncertainty in the beam direction. The error in the alignment between the target and muon monitor causes the error on the beam direction. The beam-axis is tilted by 3.637 degrees downward and this results in an asymmetric profile at the muon monitor. A correction factor was estimated using the MC simulation for the measurement of the vertical direction to account for this.

*4.4.1. Profile distortion.* The muon beam profile is reconstructed by fitting the collected charge distribution assuming it has a form of perfect Gaussian. However, the profile can be deviated from the ideal Gaussian form reflecting the geometrical shape of the upstream materials. In addition, the secondary particle, such as  $\delta$ -ray, generated at the nearby materials could further distort the observed beam profile.

The beam dump consists of multiple objects as shown in Fig. 9. The deviation of the thickness or density of objects from the design value causes a non-uniformity and may distort the muon profile. The effect was estimated with a MC simulation. In the simulation, both

the density ( $\rho$ ) and thickness ( $d$ ) of the one half (positive side in the horizontal direction) of the each dump component are adjusted up/down by their listed errors. Table 5 summarizes the adjusted components of the beam dump and the resultant shifts of the profile center. In total, a value of 0.38 cm (0.032 mrad) was assigned to the systematic error of the profile center (beam direction).

The other source of distortion of the profile is soft secondary particles ( $\delta$ -rays and  $\gamma$ s) from nearby materials. We have evaluated the effect of profile distortion due to surrounding materials in two ways. The muon monitor covers an area of  $150 \times 150$  cm<sup>2</sup> transverse to the beam-axis while the actual profile width ( $1\sigma$ ) of the muon beam is typically 100-110 cm at the monitor when the horns operate at 250 kA. Namely, the muon monitor covers  $\sim 50\%$  of the profile region. In order to check how the actual profile deviates from the ideal Gaussian shape, the ionization chamber arrays were moved by  $\pm 25$  cm to take the tail of the profile into account. Then, the fit was done for the different portions of the same profile. If the profile has a perfect Gaussian shape, the fitted result will always be same at different positions of the array. However, the result showed that there are differences in the fitted results. The maximum differences among the fitted profile centers are 1.25 cm (0.106 mrad) for the horizontal direction and 1.12 cm (0.095 mrad) for the vertical direction. During beam operation, a discrepancy of the profile center has been observed between the chamber and silicon arrays (0.55 cm in the horizontal direction and 1.77 cm in the vertical direction). This discrepancy is considered to be due to the difference of the nearby structures in-between the chamber and silicon arrays, causing the profile to be distorted differently at the chambers and silicon arrays. The most probable structure that would cause the discrepancy is the silicon moving stage just behind the silicon array (see Fig. 8). Figure 10 shows the profile center measured by the chamber array during the calibration of the silicon array where the stage was moved to be positioned at each of the silicon sensors. When the silicon moving stage cornering on the top sensors, the profile center in the vertical direction measured by the chamber array shifts by  $-1.4$  cm from the nominal case in which the stage is lowered to the bottom. This suggests nearby materials affects the beam profile at the muon monitor. The shift observed in two condition, 1.25 cm for different chamber array positions and 1.77 cm for difference in the profile center between the silicon and chamber arrays, are taken as the systematic error. Even though part of the shift may be caused by the dump core structure, we conservatively add these errors since we cannot distinguish the effects.

As discussed in Sec. 4.3, gain of the sensors are relatively calibrated with a precision of 0.4% for the ionization chambers and 0.1% for the silicon PIN photodiodes. The uncertainty in this calibration was propagated to the error in the beam direction. As a result, 0.08 cm (0.007 mrad) and 0.30 cm (0.026 mrad) for the horizontal and vertical directions respectively, were assigned to the systematic error for the profile center (beam direction).

In conclusion, the total systematic error in the beam direction due to the profile distortion was estimated to be 2.20 cm in the horizontal direction and 2.22 cm in the vertical direction. These correspond to 0.187 mrad (horizontal) and 0.188 mrad (vertical) beam direction errors.

*4.4.2. Effect of the tilted beamline against the beam dump.* The beamline is tilted by 3.637 degrees vertically while the level of the beam dump is even with the ground. (see Fig. 3). This results in asymmetric path lengths of the muons going through the beam dump with respect to the beam-axis. Thus, an asymmetric profile of the muon beam is observed

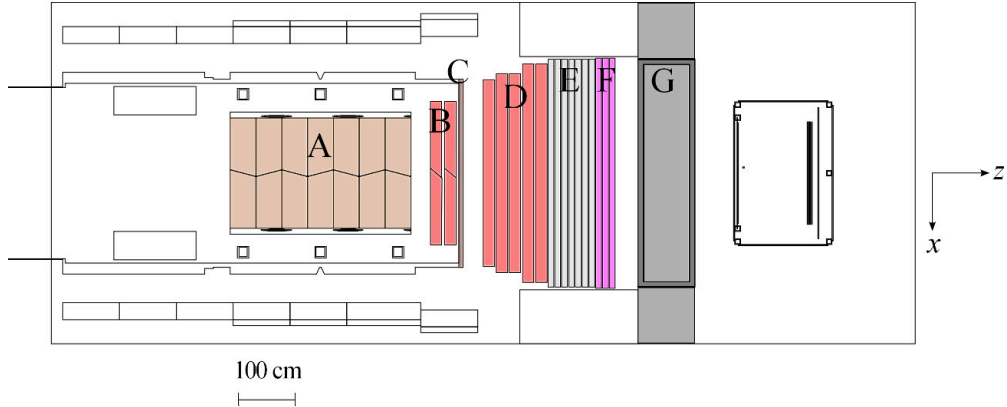


Fig. 9: Top view of the beam dump. A: graphite core. B-F: Fe plates. G: concrete wall. The beam enters from the left side.

Table 5: Density ( $\rho$ ), thickness ( $d$ ) and their uncertainties of the dump graphite core, Fe plates and concrete wall (see Fig. 9). The shift of the profile center is estimated for the case  $\rho$  and  $d$  of one half of each component are adjusted by their errors.

Material	$\rho$ (g/cm <sup>3</sup> )	$d$ (cm)	Profile center shift (cm)
A Graphite	$1.707 \pm 0.009$	$45.001 \pm 0.003$	Negligible
B Fe	$7.83 \pm 0.03$	$20.00^{+0.24}_{-0.12}$	0.107
C Fe	$7.85 \pm 0.02$	$8.00^{+0.17}_{-0.09}$	0.054
D Fe	$7.83 \pm 0.03$	$20.00^{+0.24}_{-0.12}$	0.169
E Fe	$7.8435 \pm 0.0083$	$10.083 \pm 0.033$	0.083
F Fe	$7.85 \pm 0.02$	$10.00^{+0.23}_{-0.11}$	0.126
G Concrete	$2.30 \pm 0.023$	100	0.276
Total			0.38

at the muon monitor. This causes 1.35 cm profile center shift in the vertical direction, which was estimated using MC simulation where the center of the proton beam was set to the center of the target and parallel to the beam-axis. This shift is used for the correction in the beam direction measurement and a MC statistical error of 0.22 cm (0.019 mrad) was assigned to the systematic error of the profile center (beam direction).

*4.4.3. Alignment error of the muon monitor.* For the systematic error in the beam direction measurement, alignment accuracy between the muon monitor and target is also taken into account. The alignment error mainly comes from the measurement error of the relative position of reference points between the target and muon pit, determined to be 6.1 mm for the horizontal position and 6.3 mm for the vertical position. In addition, alignment error also comes from the setting of the muon monitor (1 mm) and the target ( $< 1$  mm). The

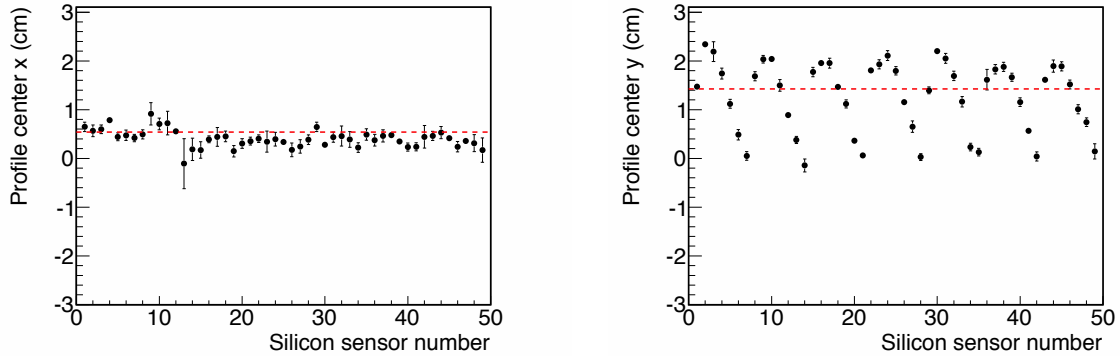


Fig. 10: Variation of the muon profile center measured by the chamber array during the calibration of the silicon PIN photodiode. The dashed line shows the profile center for the same beam condition when the silicon moving stage is lowered at the bottom (nominal position).

Table 6: Summary of the systematic error for the beam direction measurement.

Error source	Profile center		Beam direction	
	$\Delta x$ (cm)	$\Delta y$ (cm)	$\Delta\theta_x$ (mrad)	$\Delta\theta_y$ (mrad)
Profile distortion	2.20	2.22	0.187	0.188
Tilted beam	—	0.22	—	0.019
Alignment	0.63	0.65	0.054	0.055
Total	2.3	2.3	0.19	0.20

total alignment error of the muon monitor relative to the target is therefore 6.3 mm (horizontal) and 6.5 mm (vertical). Thus, the systematic error of the muon beam direction was 0.054 mrad in the horizontal direction and 0.055 mrad in the vertical direction.

*4.4.4. Summary of the systematic error on the beam direction measurement.* Table 6 summarizes the systematic error for each source. Some of these systematic errors may come from the same origin, but we conservatively take quadratic sum of these as the total systematic error. The total systematic error on the measurement of the beam direction was estimated to be 0.28 mrad ( $= \sqrt{0.19^2 + 0.20^2}$ ). Thus, the performance of the muon monitor fulfills our requirement of 0.3 mrad.

## 5. Measurement of the beam direction and beam tuning with the muon monitor

Table 7 summarizes the status of T2K beam operation since the start of physics data taking in January 2010. There have been four data taking periods (RUN 1-4) until May 2013. The repetition cycle of the proton beam has been reduced over the course of beam operations and 2.48 s was achieved for RUN 4. All three magnetic horns were operated at 250 kA except for RUN 3b where the horns were operated at 205 kA. Figure 11 shows the history of the total accumulated p.o.t., as well as the beam power. The beam power has increased gradually and

Table 7: Summary of the status of the beam operation in T2K. The second and third column shows the repetition cycle of the proton beam and the horn current, respectively. The accumulated number of p.o.t. obtained for each run is shown in the last column.

	Period	Rep. cycle (sec)	Horn curr. (kA)	Accum. p.o.t.
RUN 1	Jan. 2010 – Jun. 2010	3.52	250	$3.28 \times 10^{19}$
RUN 2	Nov. 2010 – Mar. 2011	3.2 <sup>4</sup>	250	$1.12 \times 10^{20}$
RUN 3b	Mar. 2012	2.92	205	$2.15 \times 10^{19}$
RUN 3c	Apr. 2012 – Jun. 2012	2.56	250	$1.37 \times 10^{20}$
RUN 4	Oct. 2012 – May 2013	2.48	250	$3.60 \times 10^{20}$
			Total	$6.63 \times 10^{20}$

reached 220 kW ( $1.40 \times 10^{13}$  p.p.b. with a 2.48 s repetition cycle) during RUN 4. The muon monitor plays an important role in measuring the direction and intensity of the muon beam as described in Sec. 5.2. At the commissioning stage of the experiment, the horn currents were varied from 0 kA to 250 kA to check the dependence of the muon flux on the horn current. We also varied the currents by  $\pm 1\%$  from  $\sim 250$  kA in order to check if the muon monitor is sensitive to this level of variation in the horn currents. In addition, the monitor was used as a tool for a survey of the components in the secondary beamline—this result was useful for understanding the current configuration of the baffle and target. Details of the measurement are provided in Sec. 5.5. Finally, section 5.6 describes the property of the muon beam direction with 205 kA operation.

### 5.1. Proton beam tuning with the muon monitor

Figure 12 shows a schematic view of the configuration of the components in the secondary beamline, the proton-beam monitor, as well as the muon monitor. Before hitting the target, the proton beam passes thorough proton-beam monitors placed in the primary beamline just upstream of the secondary beamline. Segmented secondary emission profile monitors (SSEM) are used for monitoring the profile center and width of the proton beam. The baffle is placed downstream of SSEM19, which is the most downstream SSEM and this plays the role of a collimator with an opening of 30 mm. An optical transition radiation (OTR) monitor [12] is placed just in front of the target and is used for the measurement of the position of the proton beam. Using the SSEMs and OTR measurements, the beam position upstream of the baffle (target) is reconstructed with an accuracy better than 0.7 mm (0.6 mm). Data at various beam position were taken to measure the correlation between the proton beam position at the target and the profile center of the muon beam at the muon monitor. As shown in Fig. 13, the profile center measured by the muon monitor is very sensitive to the position of the proton beam at the target. The angle and position of the proton beam are tuned very precisely using the correlation such that the profile center of the muon beam is centered at the muon monitor.

<sup>4</sup>3.04 sec from March 7th 2011 to March 11th 2011

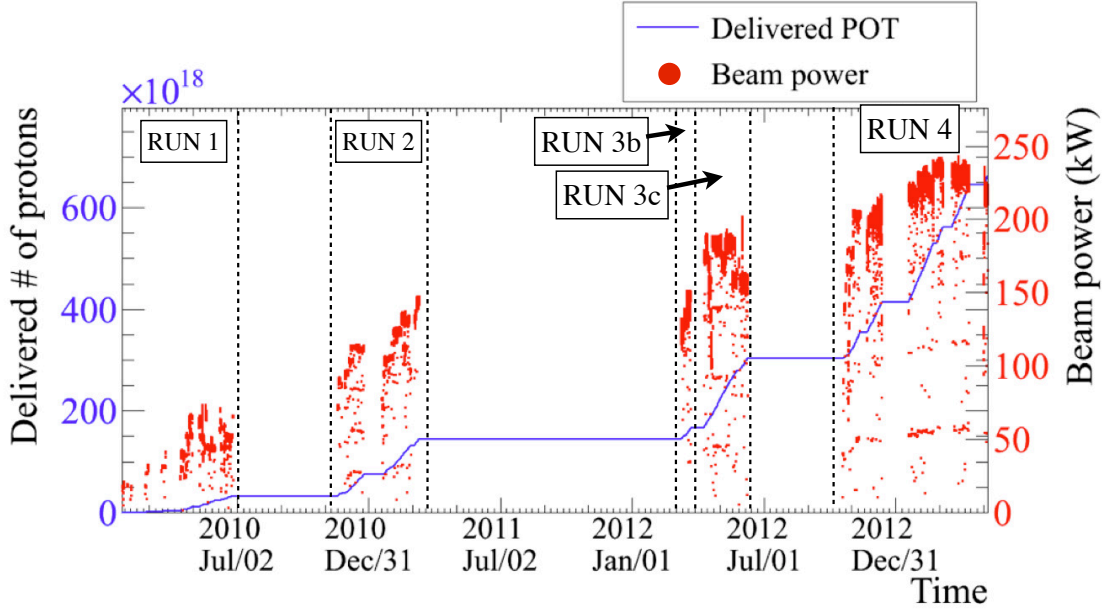


Fig. 11: History of total accumulated protons and beam power. The solid line shows the accumulated p.o.t. The dot points show the beam power.

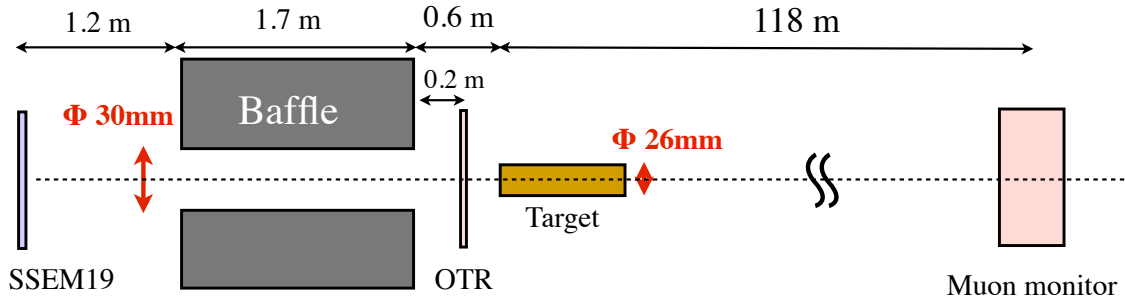


Fig. 12: Plan view configuration of the components in the secondary beamline with SSEM19 and the muon monitor.

### 5.2. Stability of the beam direction and intensity measured by the muon monitor

As described in Sec. 5.1, the proton beam is tuned using information from the muon monitor and always controlled such that the muon beam and hence the neutrino beam are on the beam-axis. Stability of response of silicon sensors is confirmed as described below. As a radiation dose at the sensor on beam-axis is expected to be twice as high as that at the edge sensor, degradation due to the radiation damage is expected to be different between these two sensors. The effect of different radiation dose can be estimated using calibration data taken in different periods, where signals from the sensors are measured at various positions (see Sec. 4.3). The difference in the signal size between the edge and center sensors was checked for different calibration data sets. We then checked if there is any significant decrease in the signal size at the center sensor where the radiation dose is highest. As a result,



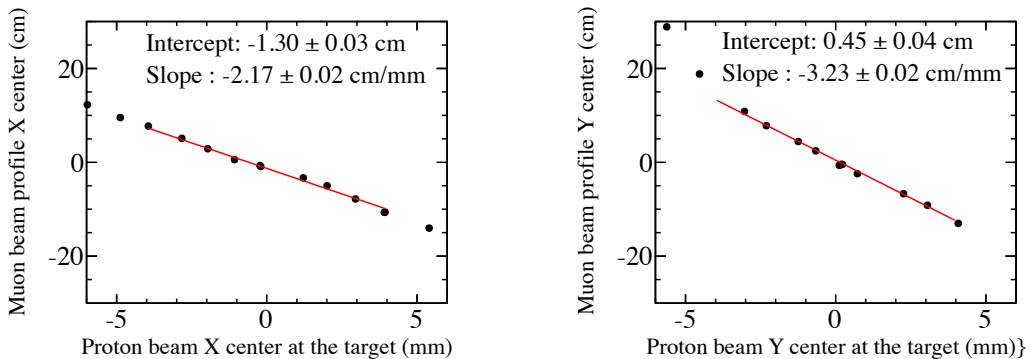


Fig. 13: Correlation between the profile center at the muon monitor and the proton beam position at the target in the horizontal (left) and vertical (right) direction. The position of the proton beam is extrapolated at the target using the measurement of the SSEMs and OTR. Fitted lines (red lines) and the results are shown in the figures. The errors on the fitted parameters are only statistical ones.

we confirmed that there was no significant decrease in the signal size after accumulating  $\sim 1.0 \times 10^{20}$  p.o.t. From this result, we ensure that the response of the sensor is stable for operation accumulating  $\sim 1.0 \times 10^{20}$  p.o.t., which is a typical value of p.o.t. obtained in each run period (Run 1-3). For Run 4 operation where more than  $1.0 \times 10^{20}$  p.o.t. was accumulated, we rely on the result from the beam test and assumption discussed in Sec. 3.2. Figure 14 shows the daily stability of the muon beam as measured by the muon monitor. The profile center measured by the silicon and chamber array is shown in the top and middle sections respectively. As shown in the history of the beam direction, most of the events lie within 0.3 mrad except for RUN 1 and RUN 3b. After the RUN 1 operation, the center position of the muon monitor was found to be mistakenly mis-aligned by -2.5 cm in the vertical direction. This mis-alignment was taken into account for the beam tuning from the RUN 2 operation onwards. The magnetic horns were operated at 205 kA during the RUN 3b operation. Unlike in the case of 250 kA operation, the profile center of the muon beam was shifted during 205 kA operation even though the proton beam position was tuned to the center at the target using the correlation shown in Fig. 13. The direction and intensity of the neutrino beam have also been measured by INGRID and this result is shown in Fig. 15, with the neutrino event rate having been stable over the majority of the run period. The beam direction measured by INGRID shows a different tendency from that of the muon monitor during the RUN 3b operation. However, all of the spills were within 1.0 mrad for both the muon and neutrino beams. In addition, most of the spills were controlled well within our 0.3 mrad requirement. Table 8 summarizes the average and RMS of the profile center and total collected charge. Although the profile center deviated largely during RUN 3b, we achieved good stability in the beam direction over the entire period. The total collected charge was also kept stable and the RMS was less than 1.0%.

Table 8: Average of the profile center and total collected charge measured by the muon monitor for each T2K run period. The numbers in parentheses denote the RMS.

Period	Silicon array			Ionization chamber array		
	Profile center		Total collected charge	Profile center		total collected charge
	X (cm)	Y (cm)	(nC/10 <sup>12</sup> p.o.t.)	X (cm)	Y (cm)	(nC/10 <sup>12</sup> p.o.t.)
RUN 1	-0.1 (0.62)	-3.8 (0.53)	32.7 (0.7%)	0.4 (0.47)	-2.0 (0.47)	0.939 (0.7%)
RUN 2	0.2 (0.42)	-1.9 (0.48)	32.8 (0.8%)	1.0 (0.45)	-0.5 (0.46)	0.922 (0.7%)
RUN 3b	4.8 (0.60)	4.2 (1.52)	21.7 (0.7%)	5.9 (1.11)	6.7 (2.18)	0.640 (0.7%)
RUN 3c	-0.4 (0.38)	0.1 (0.41)	32.0 (0.7%)	0.6 (0.46)	1.1 (0.47)	0.942 (0.6%)
RUN 4	-0.3 (0.33)	-0.8 (0.47)	32.4 (0.8%)	0.8 (0.34)	0.9 (0.66)	0.954 (1.0%)

### 5.3. Resolutions for the direction and intensity measurements of the muon beam

The direction and intensity of the muon beam can vary spill-by-spill due to the fluctuations in the proton beam direction and in the horn current. The resolution of the variation in the direction and intensity measurement by the muon monitor was estimated using two independent detectors, i.e. the silicon and chamber arrays in order to reduce the effects from intrinsic beam fluctuations. For the beam direction, we took the difference in the measured profile center between the silicon and chamber arrays (see left in Fig. 16). For the beam intensity, we took a ratio of the total collected charge measured by the silicon array to that measured by the chamber array (see the right in Fig. 16). Both the resolutions for the direction and intensity measurement are actually convoluted signals from the chamber and silicon sensors. As the size of a signal from the silicon array is 30 times larger than that from the ionization chambers, the resolution at lower intensity is limited by the resolution of the ionization chambers. The resolutions become better as the proton beam intensity increase. As a result, we achieve good resolutions of  $< 3.0$  mm for the direction and  $< 0.1\%$  for the intensity measurement when the beam intensity is above  $\sim 0.5 \times 10^{13}$  p.p.b.

### 5.4. Dependence of the muon yield on the horn current

Increasing the horn currents results in focusing more charged pions and producing more intense muon and neutrino beams. The focusing of pions can be confirmed by the change of muon flux, which is measured as the collected charge in the muon monitor. During beam operation, we tested how the collected charge changes by varying the horn currents from 0 kA to 250 kA. Figure 17 shows the total collected charge measured by the silicon array for various horn currents. When all of the horns are operated at 250 kA, the collected charge are increased by a factor of 4 compared with the case of 0 kA horn current setting. We also varied the horn current within  $\pm 1\%$  (2.5 kA) and checked the effect on the collected charge. This result is shown in Fig. 18. When the Horn1 current was varied by  $\pm 1$  kA from 250 kA while fixing the Horn2 and Horn3 currents at 252 kA, the collected charge measured by the silicon array varied by 0.40% (left in Fig. 18). Subsequently, Horn2 and Horn3 currents were simultaneously varied by  $\pm 1\%$  from  $\sim 250$  kA while fixing the Horn1 current at 248 kA. This resulted in a 0.33%/kA change in the collected charge (right in Fig. 18). As described in Sec. 5.3, the muon monitor has a resolution of 0.1% in the beam intensity measurement. Thus, the monitor is sensitive to variations of  $\sim 0.3$  kA in either Horn1, or Horn2 and Horn3

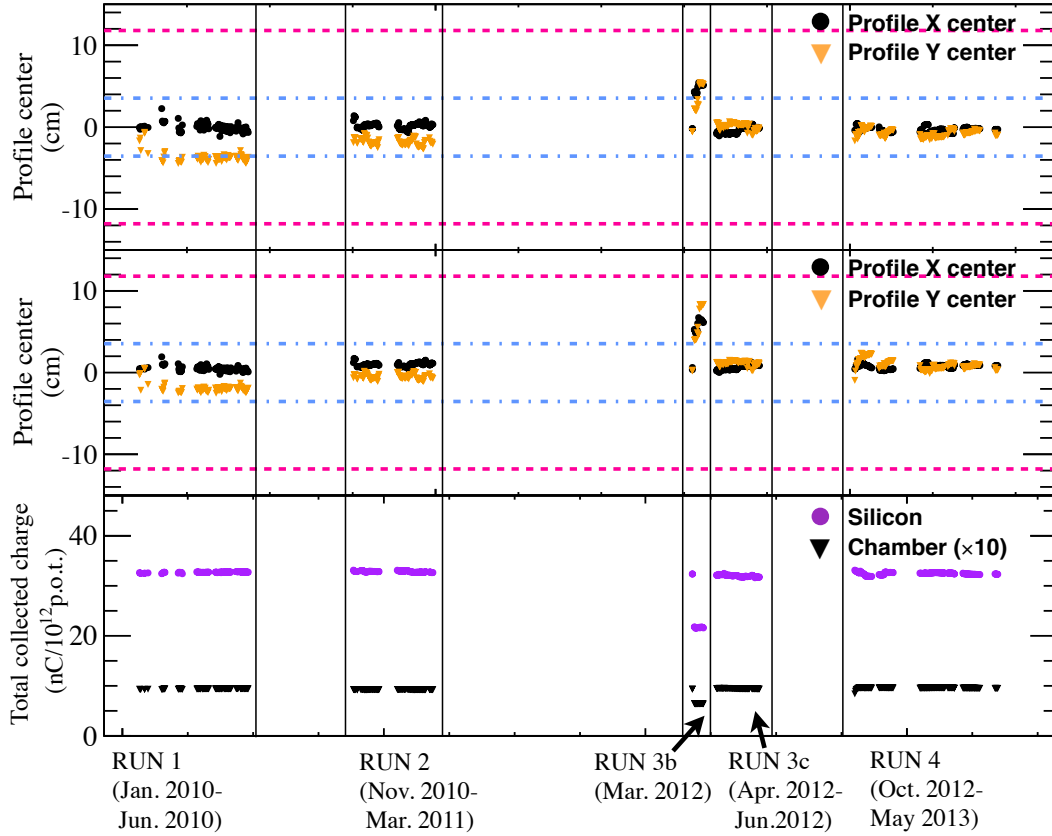


Fig. 14: Daily stability of the muon beam measured by the muon monitor. The profile center measured by the silicon and chamber array is shown in the top and middle respectively. The profile center values corresponding to a beam direction of 1.0 mrad and 0.3 mrad are also displayed as pink and blue dashed lines, respectively. The total collected charges measured by the silicon and chamber (scaled up by 10 times) are shown in the bottom of the figure.

combined. These results show that the muon monitor is also useful for monitoring the horn currents.

### 5.5. Survey of the secondary beamline.

The configuration of the components in the beamline might be changing due to the sinking of the ground. In addition, the Great East Japan Earthquake in 2011 resulted in movement of many of the components [9]. The muon monitor has also played an important role in confirming the alignment of the secondary beamline. Ideally the relative center positions between these two components, the proton beam will hit the baffle (collimator) and will not produce secondary particles in the target effectively. In addition, the miss-steered beam, which is not collimated properly by the baffle, would result in hitting downstream components. However, it is impossible to survey the instruments with a visual inspection

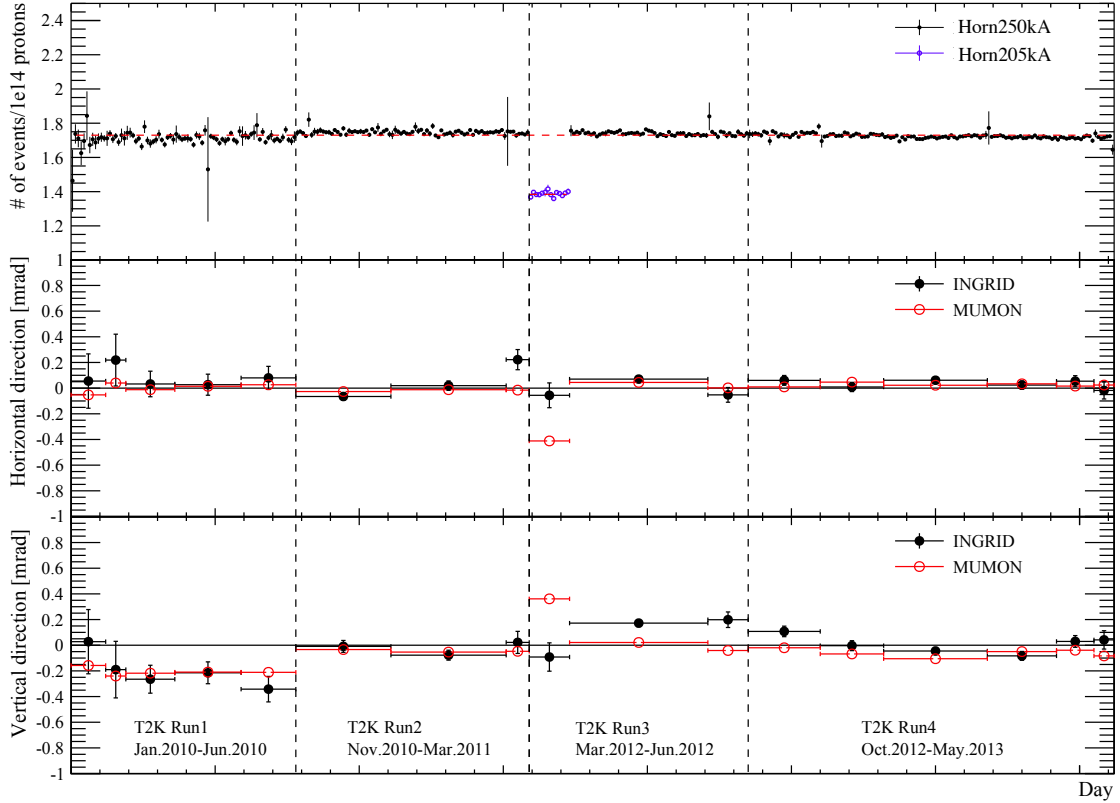


Fig. 15: Top: Neutrino event rate per  $10^{14}$  p.o.t. measured by INGRID (points) with the mean value (dashed line). Middle and Bottom: Beam direction measured by the muon monitor (red open circle) and INGRID (black circle) in the horizontal and vertical direction respectively. The error bar represents the statistical error. In this figure, a sign is reversed for the horizontal direction measured by the muon monitor so that the x-coordinate for the muon monitor matches that for INGRID.

during beam operation because they are inside the helium gas volume enclosed by the helium vessel. We therefore conducted the survey using the proton beam during operation just after the recovery work for the earthquake. The proton beam size was set 2.3-2.8 mm during the survey run while the nominal size is  $\sim 4$  mm. As shown in Fig. 12, the baffle has a beam hole of 30 mm, while the target has a diameter of 26 mm. Namely, there is a radial gap of 2 mm between the baffle and target. If the alignments of these two instruments are perfect, the proton beam interacts less with the target when passing through the gap. Then the contribution of the muons from interactions at the dump increases. This results in a narrower muon beam at the muon monitor. Figure 19 shows the profile width of the muon beam at the silicon array, obtained by scanning the proton beam position at the baffle in horizontal (left) and vertical (right) axes. The expected position of the 2 mm gap between the baffle and target is expressed as the red shaded region ( $-15 \sim -13$  mm and  $13 \sim 15$  mm) in the figure. As shown in Fig. 19, the profile widths have minimums around the gap in both horizontal and vertical axes. Fitting to these dips with a quadratic function was performed

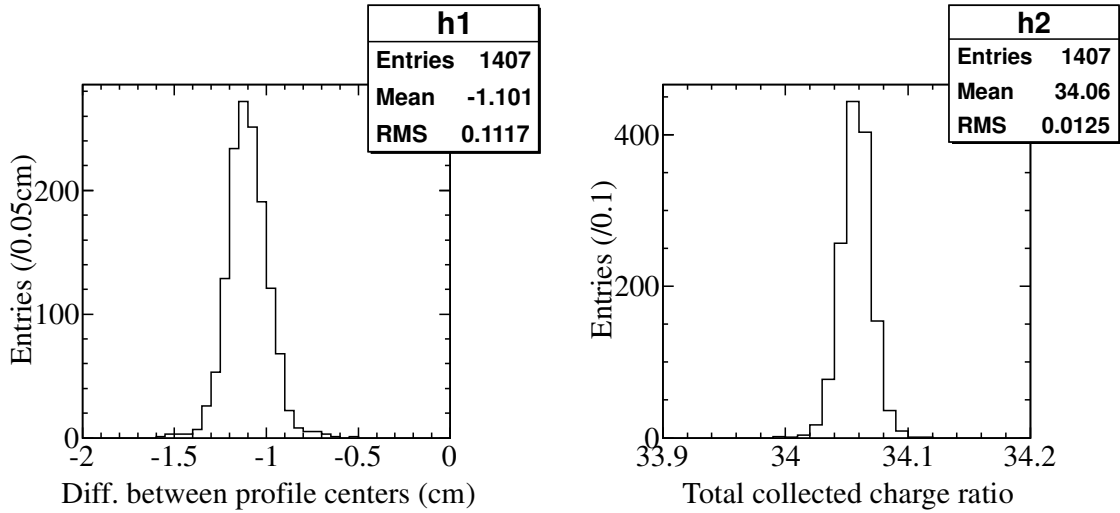


Fig. 16: Obtained resolution of the variation in the direction (left) and intensity (right) measurement by the muon monitor. For the beam direction, the difference in the measured profile center between the silicon and chamber arrays was measured. For the beam intensity, we took a ratio of the total collected charge measured by the silicon array to that measured by the chamber array. These results were obtained using beam data with 1 hour operation and  $1.3 \times 10^{13}$  p.p.b. of the proton beam intensity.

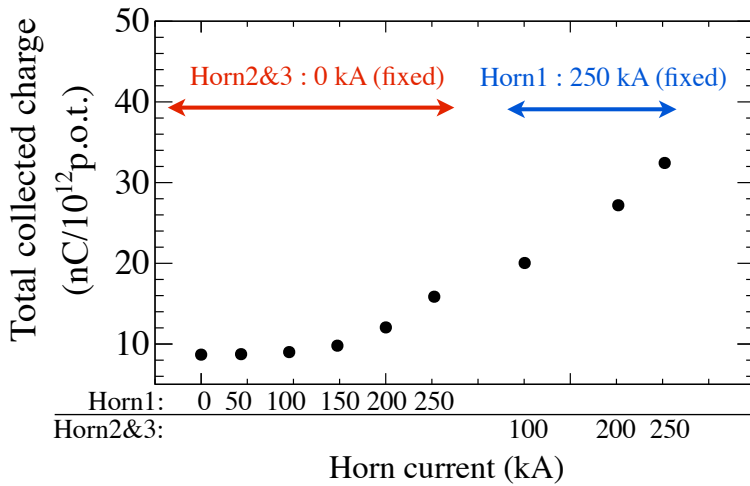


Fig. 17: Dependence of the total collected charge for different combination of horn currents.

to extract the actual gap position. The fitted dips are situated within the expected position of the 2 mm gap between the baffle and target.

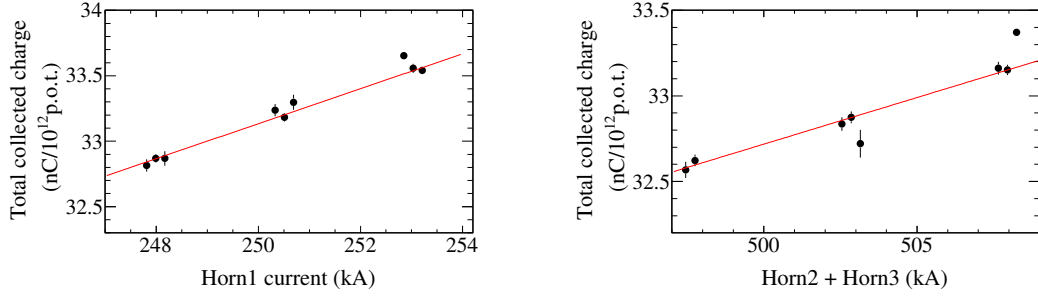


Fig. 18: Dependence of the total collected charge on the horn current variation. Left: the Horn1 current was changed by  $\pm 1\%$  (2.5 kA) from the nominal value (250 kA) while fixing the Horn2 and Horn3 currents at 252 kA. Right: the Horn2 and Horn3 currents were simultaneously changed by  $\pm 1\%$  (2.5 kA) from the nominal values while fixing the Horn1 current at 248 kA.

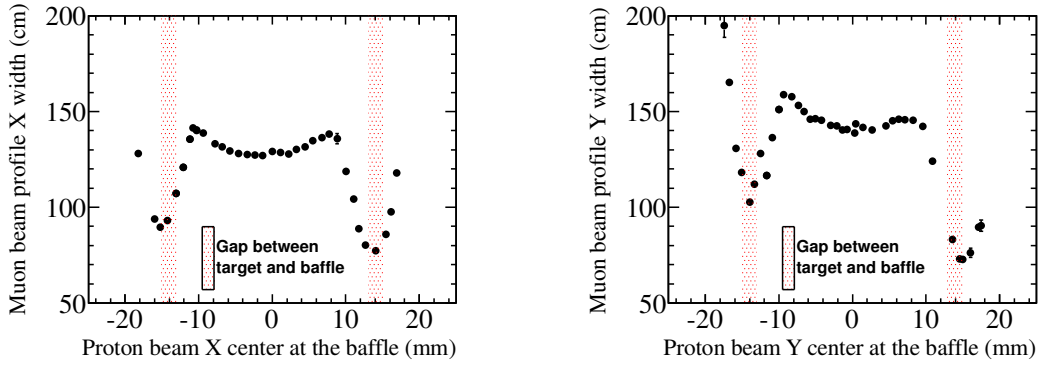


Fig. 19: Profile width of the muon beam at the silicon array obtained by scanning the proton beam at the baffle in horizontal (left) and vertical (right). The expected position of 2 mm gap between the baffle and target is expressed as the red shaded region ( $-15 \sim -13$  mm and  $13 \sim 15$  mm). All of the horn currents are set to 0 kA during the data taking.

### 5.6. Property of the muon beam direction with 205 kA operation

In order to understand property of the muon beam direction during the 205 kA operation, we scanned the proton beam at the target and compared the result with that from the 250 kA operation. Figure 20 shows the correlation between the profile center at the silicon array and the proton beam position at the target. As seen in the figure, the correlation is negative at the 250 kA operation. Whereas it becomes positive at the 205 kA operation. The reason is considered as follows. An off-center proton beam produces secondary particles asymmetrically with respect to the beam-axis because of different path lengths through the target. In the case of 0 kA horn current setting, particles in the opposite direction of the off-center beam are more attenuated in the target (see left in Fig. 21). The muon beam would then be directed in the same direction as the off-center beam, resulting in the positive

Table 9: Fitted gap position between the baffle and target. The error is statistical.

	Scan in horizontal		Scan in vertical	
	$x < 0$	$x > 0$	$y < 0$	$y > 0$
Fit result (mm)	$-15.0 \pm 0.04$	$13.7 \pm 0.04$	$-14.1 \pm 0.03$	$14.9 \pm 0.11$
Fit range (mm)	$-17.0 \sim -13.0$	$11.5 \sim 15.5$	$-16.0 \sim -13.0$	$13.0 \sim 16.5$

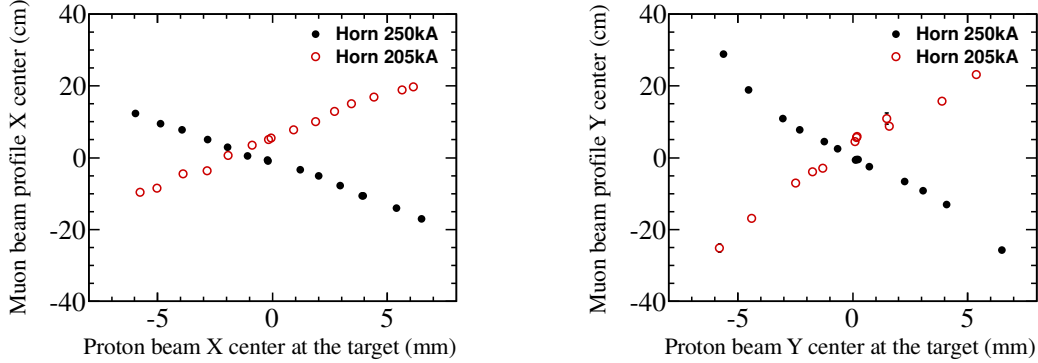


Fig. 20: Correlation between the profile center at the silicon array and the proton beam position at the target for the 250 kA (black) and 205 kA (red) operation.

correlation. On the other hand, when the horn currents are tuned on and the focusing becomes stronger, this results in the negative correlation between the profile center at the muon monitor and the proton beam position at the target. This is considered as follows. When the proton beam is off-center at the target, differences arise in the exit points from the target between secondary particles. For example, if the proton beam hits the target in the positive direction, the secondary particles generated exit in the positive direction from the target faster than ones generated in the negative direction. Those which exit the target faster experience a larger Lorentz force and are therefore more focused (see the right in Fig. 21). Thus, the muon beam would be directed in the opposite direction, i.e. negative direction. The MC simulation was also used to confirm the dependence of the profile center position of the muon beam on the proton beam position at the target with different horn currents. The result also showed the correlation is positive at the 205 kA operation. In addition, correlation is lost for some horn current value between 205 kA and 250 kA. This means that the profile center of the muon beam is no longer sensitive to the proton beam position at the target for some horn current value between 205 kA and 250 kA.

## 6. Absolute muon yield measurement by emulsion detector

The particles arriving at the muon monitor are expected to be a mixture of muons and some lower energy components, namely electrons and gammas as shown in Table 1. Since the standard detectors of the muon monitor, the silicon detectors and the ionization chambers, are designed to obtain the profile of the muon beam by measuring the integrated ionization

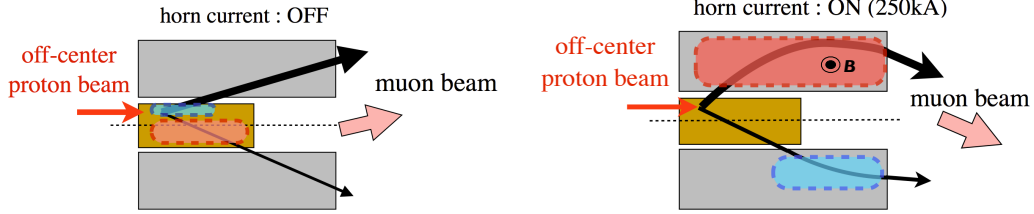


Fig. 21: Explanation of changes in the direction of the muon beam when the horn current is turned off (left) and on at 250 kA (right).

in their active volumes, the measured profile is a convolution of all components in Table 1. However, the understanding of the muon flux is a key issue to understand the nature of the beam. Therefore, it is important to measure the absolute muon flux and compare it with the model. In order to complement the muon monitor measurement and to diagnose the absolute muon flux, a set of emulsion detectors is temporarily inserted during the period of commissioning.

The emulsion detector has a high spatial resolution, down to tens of nano-meters, allowing a 5D reconstruction of particle trajectories, 3 positions ( $X, Z, Y$ ) and 2 angles ( $\tan\theta_x, \tan\theta_y$ ), for particle densities of up to  $10^6$  particles/cm<sup>2</sup>. Furthermore, by employing a proper detector structure, it can successfully reject the low energy components by their multiple Coulomb scattering inside the detector materials.

The emulsion film used for this measurement is the recent standard emulsion film, so-called OPERA film [13], which has two sensitive 44  $\mu\text{m}$  emulsion layers on both sides of a plastic base (205  $\mu\text{m}$  thick) and the thickness of the film in terms of radiation length is 0.003  $X_0$ . In order to reduce the background tracks accumulated in the emulsion film, a *refreshing* treatment [13] was previously applied. All films were put in a climate chamber and remained at  $T=28^\circ\text{C}$  with R.H.=98% for 6 days, and then dried at  $T=20^\circ\text{C}$  with R.H.=50% for 1 day. The emulsion detector module consists of 8 emulsion films shaped into 6 cm  $\times$  5 cm dimensions and the horizontal array of 7 modules (25 cm spacing) was placed on the neutrino beam-axis just downstream of the ionization chambers to measure the absolute muon yield.

In addition to the above detector array, another detector dedicated to measuring the momentum distribution of muons was also placed at the center of neutrino beam. These muon momentum measurements will be the subject of future publication.

The data readout of emulsion films is performed with the OPERA scanning microscopes [14] and the tracks crossing several films are reconstructed by the FEDRA emulsion data analysis framework [15]. The reconstructed tracks which have at least 4 hits out of 8 films, with the most upstream hit existing among the first 4 films are selected.

The performance of the detector module for the flux measurement is also checked with a Geant4-based MC simulation (G4). The flux input, described in Sec. 7, is propagated through the detector by G4 with the detection efficiency described later.

The energy distributions of the input fluxes and the reconstructed particles are shown in Fig. 22 on the left, as a stacked histogram with black and dashed red lines. An application of the angular acceptance of  $\tan\theta < 0.3$  (where  $\theta$  is the angle from the normal vector of the film surface) can effectively reduce the low energy components because the track angles



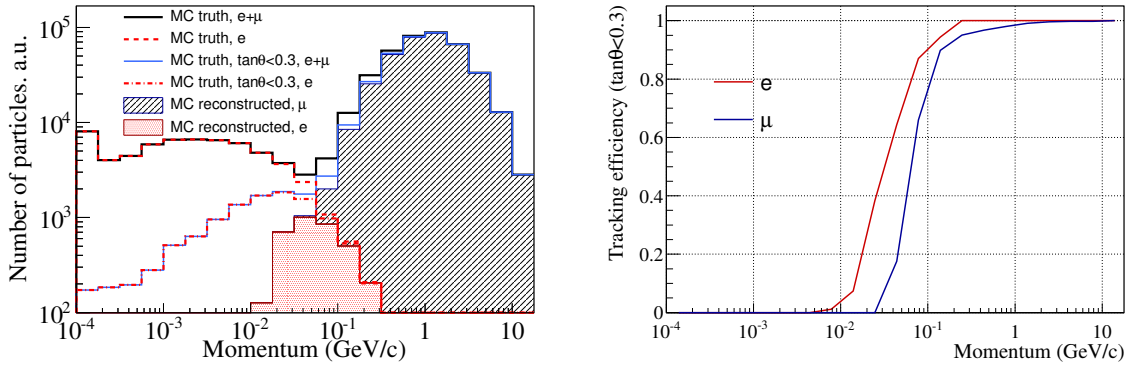


Fig. 22: Left: Momentum distribution of the input fluxes and the reconstructed particles. Right: tracking efficiency for the particles in an angular acceptance of  $\tan \theta < 0.3$ .

Table 10: Horn current, the number of shots, and p.o.t. for each exposure time.

Exposure	Horn current	# of shots	pot
A	250 kA	1	$1.949 \times 10^{11}$
B	0 kA	2	$1.984 + 1.951 = 3.935 \times 10^{11}$

of low energy components have less correlation with the beam angle (blue and fine dashed red lines). The reconstructed tracks are shown as a filled stacked histogram; the additional reduction of low energy components is achieved via their multiple Coulomb scattering in the 8 films by requesting a stringent angular matching between the films. The track reconstruction efficiencies for muons and electrons are given in Fig. 22 on the right, as a function of their momenta. The overall detection efficiency for muons is estimated to be 98.0% with respect to the muons in the angular acceptance or 94.2% for muons in all angular space. The contamination by electrons is expected to be as small as 1.0% with respect to the number of muons reconstructed in the angular acceptance.

The emulsion detectors were exposed to a low intensity beam twice with the different horn current settings, see Table 10. The films were then photo-developed.

For each film, the data is taken from a  $2 \text{ cm}^2$  area at the center of film. The relative alignments between the films are found by using the beam tracks themselves with sub-micron precision. After the track reconstruction, an effective area of  $1 \text{ cm}^2$  at the center of film is used to compute the flux. An example of the reconstructed tracks is shown in Fig. 23 on the left, and the angular distribution on the right.

The detection efficiencies of each film and module are measured using the reconstructed tracks in the module, counting the number of missing hits in the film for the tracks crossing the film and are shown in Fig. 24. The tracking efficiency of each module is then computed by taking account of the efficiencies of individual films in the module. The average track detection efficiencies for high energy particles, where multiple Coulomb scattering does not play a role for the inefficiency, are calculated to be higher than 99.5% for all modules. The flux data is corrected by the track detection efficiency module-by-module in the later analyses.

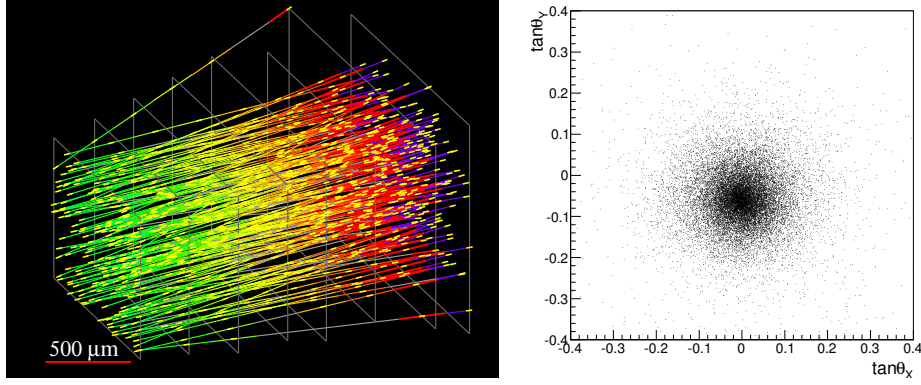


Fig. 23: Left: Example of reconstructed tracks entering in the  $1 \times 1 \text{ mm}^2$  surface in the center module when the horn is operated at 250 kA. The color of lines shows the depth in the module. Right: The measured angular distribution in the same detector. Each dot corresponds to the individual track angle.

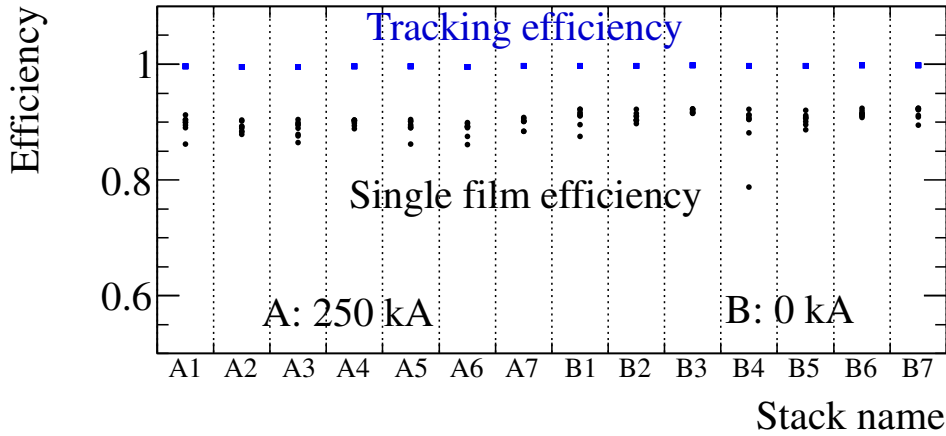


Fig. 24: Single film and tracking efficiencies for all films and modules. The efficiency is computed using all tracks with the angular acceptance of  $\tan \theta < 0.3$ .

The measured muon flux normalized to  $4 \times 10^{11}$  p.o.t. is shown in Fig. 25. For each data point, the systematic uncertainty of 2%, which were estimated from the measurement reproducibility test<sup>5</sup>, is taken into account in addition to the statistical error. The flux data is fitted with a Gaussian function and the measured muon fluxes at the profile center are  $(1.09 \pm 0.01) \times 10^4 \text{ tracks/cm}^2 / 4 \times 10^{11} \text{ p.o.t.}$  when the horns are not operated and increased to  $(4.06 \pm 0.05) \times 10^4 \text{ tracks/cm}^2 / 4 \times 10^{11} \text{ p.o.t.}$  when the horns are operated at 250 kA. The  $1\sigma$  widths of the flux profiles are measured to be  $122.4 \pm 6.5 \text{ cm}$  and  $105.6 \pm 4.1 \text{ cm}$ , respectively.

<sup>5</sup> Two flux modules were placed one after the other and exposed to the beam. The difference of number of muons between those modules was assigned to the systematic error.

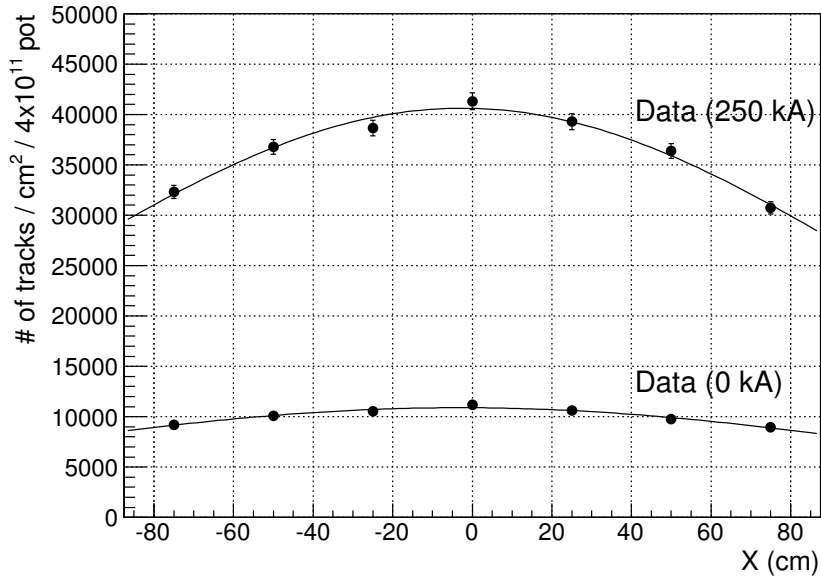


Fig. 25: Measured muon flux with fitted lines represented as solid curves. Error bars denote statistical and systematic ones.

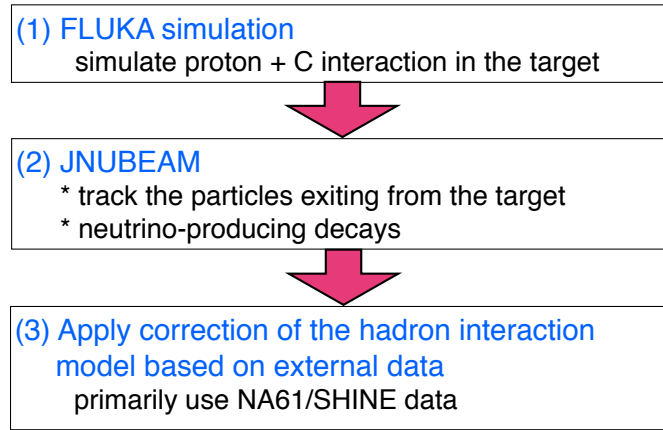


Fig. 26: Flow diagram of the flux prediction.

## 7. Comparison of the muon yield with prediction based on tuned-simulation

As described in Sec. 4.2, T2K uses FLUKA2008 for the simulation of the hadronic interaction in the graphite target and the kinematic information for the particles is then transferred to the JNUBEAM simulation. Hadronic interactions in the JNUBEAM simulation are treated with GCALOR. For a precise prediction of the neutrino and muon flux, T2K corrects the model based on hadron interaction data provided by external experiments, primarily relying on the NA61/SHINE measurements [16]. A flow diagram for the precise estimation of the muon flux is shown in Fig. 26. This section first describes how the muon flux is predicted in Sec. 7.1. Systematic errors of the prediction summarized in Sec. 7.2. The result is then compared with the measurement from the emulsion data in Sec. 7.3.

### 7.1. Correction of the muon flux

In order to make a prediction based on the external hadron-interaction data, we use the method developed for the T2K flux prediction [9]. Here, we briefly summarize the procedure. Following quantities modeled in FLUKA2008 and GCALOR are corrected based on the external data,

- (1) interaction rates for  $p$ ,  $\pi^\pm$  and  $K^\pm$ , and
- (2) differential production of  $\pi^\pm$ ,  $K^\pm$  and  $K_L^0$  in the interaction of protons on the target.

The NA61/SHINE measurement provides both the differential production and the interaction rate [17, 18], which are primarily used for the prediction of the neutrino and muon flux. Other experimental data are used to compensate for the measurement of NA61/SHINE [19, 20, 21].

The hadronic interaction rate is defined as a cross section calculated by subtracting the cross section for the quasi-elastic scattering process ( $\sigma_{qe}$ ) from the total inelastic cross section ( $\sigma_{inel}$ ):

$$\sigma_{prod} = \sigma_{inel} - \sigma_{qe} \quad (5)$$

Most of the data provides  $\sigma_{inel}$ . Thus,  $\sigma_{qe}$  are subtracted from  $\sigma_{inel}$  to extract  $\sigma_{prod}$ . Since the prediction of FLUKA2008 was found to be good agreement with the data, this correction is applied only to  $\sigma_{prod}$  in GCALOR.

Figure 27 shows the phase space of the parent  $\pi^+$  contributing to the muon flux at the muon monitor when the horn currents are set at 250 kA (left) and 0 kA (right). Most of the phase space is covered by the NA61/SHINE data for the 250 kA operation. On the other hand, only  $\pi^+$ s in the forward angle regions reach the muon monitor for the 0 kA operation. This results in only around 30% coverage by the NA61/SHINE data. Most of the  $K^+$  contributing to the muon flux are not covered by the NA61/SHINE data<sup>6</sup>. The differential production depends on the incident particle momentum,  $p_{in}$ , and target nucleus,  $A$ . For secondary  $\pi^\pm$ s produced by 31 GeV/c protons in the phase space covered by NA61/SHINE data, corrections are directly applied using the NA61/SHINE data. The corrections for tertiary pion production from secondary particles and for the production at materials ( $A$ ) other than graphite are obtained with extrapolations from the NA61/SHINE data assuming momentum and A-dependent scaling [22, 23, 24, 25].

The correction for the production of  $K^+$  and  $K^-$  in the phase space not covered by the NA61/SHINE data is estimated with other experimental data [19, 20]. For the hadrons in phase space uncovered by any experimental data, the corrections are no longer applied.

Figure 28 and Table 11 show the absolute muon flux at the emulsion after the correction of the hadron productions. As a result of the correction the absolute muon flux is increased by about 20% (1.9% by the production cross section, 14.8% by the pion and 3.1% by the kaon production tuning).

---

<sup>6</sup>The correction of the flux was performed using results from the NA61/SHINE measurement in 2007. NA61/SHINE also collected data in 2009, where statistics increased by an order of magnitude as compared to the 2007 data and a phase space coverage was enlarged. Therefore the flux is expected to be predicted more precisely with the 2009 data.

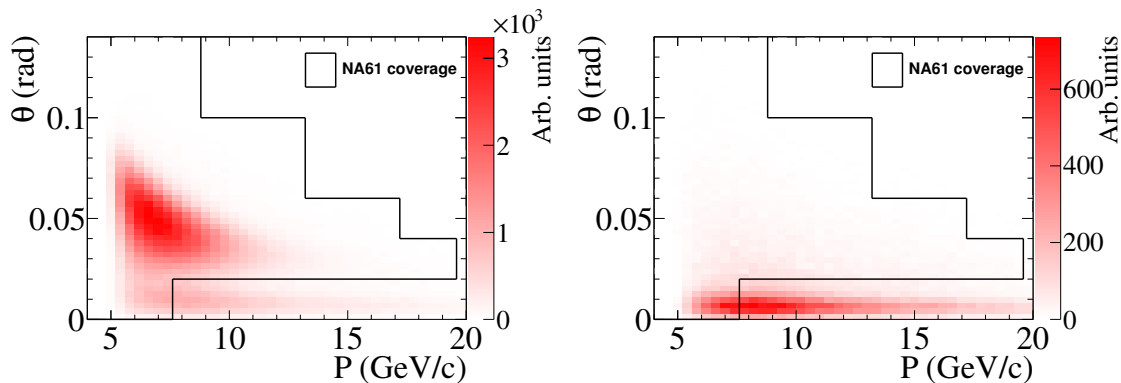


Fig. 27: Phase space of the parent  $\pi^+$ s contributing muon flux at the muon monitor when the horn currents are operated at 250 kA (left) and 0 kA (right). NA61 coverages shown in these figures correspond to the 2007 data.

Table 11: Predicted muon flux at the emulsion with 250 kA horn current. The second and third rows show the fitted peak and sigma of the profile of the muon beam.

	Flux after correction
Muon flux ( $/\text{cm}^2/10^{12}\text{p.o.t.}$ )	$9.72 \times 10^4$
Fitted peak of the profile ( $/\text{cm}^2/10^{12}\text{p.o.t.}$ )	$1.09 \times 10^5$
Fitted sigma of the profile (cm)	$100.6 \pm 1.8$

## 7.2. Systematic error on the flux prediction

The systematic error on the muon flux prediction originates from uncertainty in the hadron production and measurement error of the proton beam, horn current, and alignment of the target.

*7.2.1. Uncertainty of the hadron production.* The systematic error on the production cross section is dominated by the uncertainty of the quasi-elastic subtraction. This assumption is based on discrepancies in the production data among data sets [9].

The systematic error of the pion or kaon differential production comes from:

- (1) measurement error of the pion/kaon differential production,
- (2) uncertainty in the momentum or target scaling,
- (3) uncertainty from the pion/kaon production in the phase space not covered by data.

In addition to uncertainties listed above, the systematic error on the muon flux also arises from uncertainty in secondary nucleon productions. The error is basically estimated using other experimental data sets [19, 20]. For the region where the incident protons undergo with a small momentum transfer, we assign 100% error to the production due to the lack of relevant data.

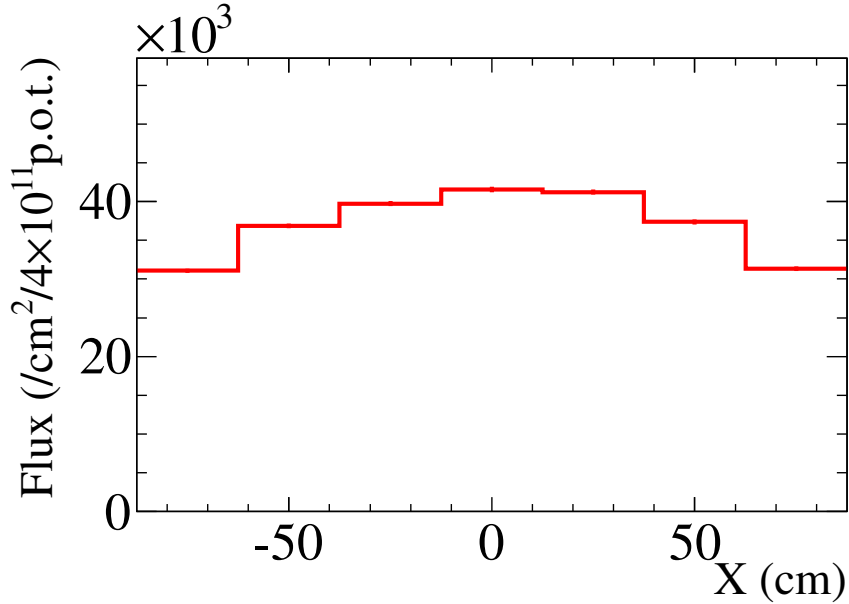


Fig. 28: Predicted muon flux at the emulsion for the 250 kA horn operation.

The muon flux is also generated from the interactions at the beam dump (C) and it contributes about 4% of the total flux as shown in Table 4. We test correction of the proton-beam production at the dump and it results in decreasing the muon flux by 0.7%. The change of 0.7% is assigned to the systematic error on the muon flux.

The muon flux is also generated from decays of  $\Lambda$ ,  $\Sigma$  or other particles whose productions are not corrected. According to the MC simulation, 0.6% of the muons come from such particles. Since there is no relevant data for such production, we conservatively assign a 100% error on the production. In addition, 0.6% of muons come from decays of quaternary particles, which are not corrected at this stage because of the small contributions to the muon flux. A 100% error is conservatively assigned to the decay mode. Finally we take account of 1.2% for the systematic errors from these productions.

In total, we attribute 13.4% of the systematic error in the muon flux to uncertainty in the hadron production and summarize those errors in Table 12.

*7.2.2. Uncertainty of the proton beam measurement.* A trajectory and optics of the proton beam are measured by the proton-beam monitors placed in the primary beam line as described in Sec. 2. In the MC simulation, the parameters of the proton beam are varied within those errors attributing to the measurement errors from the proton beam monitors. The resultant variation of the muon flux (0.9%) is then estimated at the muon monitor and is taken as the systematic error on the muon flux. In addition, 2.6% error in the p.o.t. measurement, which mainly originates from the calibration accuracy of the beam monitor, is assigned to the error in the muon flux. In total, we take account of 2.8% for the systematic error on the muon flux.

Table 12: Systematic errors on the muon flux due to uncertainty in the hadron production

Error source	Error size
Pion production	9.0%
Kaon production	1.3%
Production cross section	9.1%
Secondary nucleon production	3.6%
Dump interaction	0.7%
Decays from $\Lambda$ , $\Sigma$ , and quaternary particles	1.2%
Total	13.4%

*7.2.3. Uncertainty of the absolute horn current.* During beam operation, the monitored values of the horn current were found to be drifted by 2%, 5 kA. the drift is considered to be mainly due to the temperature dependence in the hardware monitoring. In the MC simulation, the horn currents are varied by 5 kA from the nominal values (=250 kA). The variation of the muon flux, 3.6%, is then taken as the systematic error on the muon flux.

*7.2.4. Uncertainty of the target alignment.* The rotation of the target with respect to the horn-axis was surveyed and was measured to be 1.3 mrad (0.1 mrad) in the horizontal (vertical) direction. The effect of the target alignment is estimated by rotating the target in the simulation according to the measured values described above. The resultant variation of the muon flux, 0.5%, is assigned to the systematic error.

*7.2.5. Skin effect in the magnetic horns.* Since the horn current is applied as pulses of about 1 ms, the current would flow only around the surface of the conductor due to the skin effect. However, the present MC simulation assumes a flat current density. To estimate the size of the skin effect, the magnetic field in the simulation is modified by taking the skin depth into account. The modification results in decreasing the muon flux by 2.0%. The change is assigned to the additional systematic error.

*7.2.6. Summary of the systematic error on the absolute muon flux.* Table 13 summarizes the systematic error on the absolute muon flux measurement. Finally we assigned a total of 14.3% error to the absolute muon flux. In the case of 0 kA horn current setting, the systematic error cannot be fully evaluated because the phase space of pions (kaons) is poorly covered by data. This may result in a large error size for the muon flux. From these reasons, we evaluated the systematic error only for the 250 kA operation.

### *7.3. Comparison with the emulsion measurement*

Figure 29 shows the comparison of the reconstructed profile of the muon flux at the emulsion between the measurement and prediction where the hadron production is corrected as described in Sec. 7.1. Both of the profiles are obtained at 250 kA horn operation. Table 14 summarizes comparisons in the muon flux at the emulsion detectors between the data and prediction. In the case of the 250 kA operation, the ratio of the measured muon flux to the prediction is  $0.971 \pm 0.143$ . The data and prediction agrees quite well. In case of the 0 kA operation, there is about a 10% discrepancy in the flux between the measurement and

Table 13: Summary of the systematic error on the absolute muon flux.

Error source	Error size
Hadron production	13.4%
Proton beam	2.8%
Absolute horn current	3.6%
Target alignment	0.5%
Horn skin effect	2.0%
MC statistics	0.3%
Total	14.3%

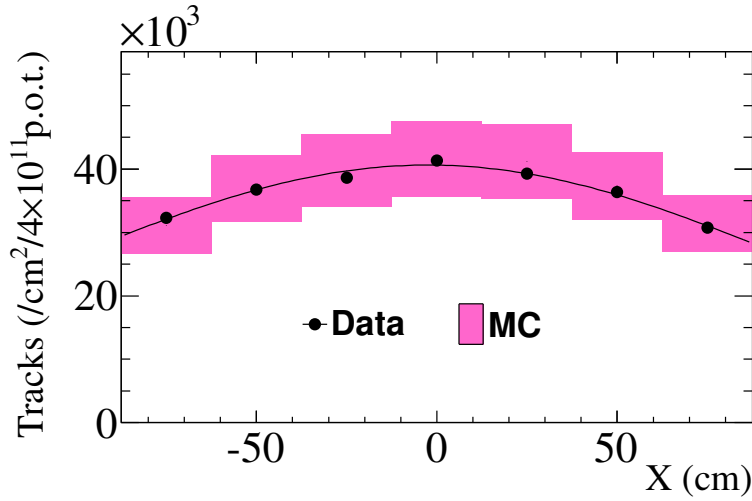


Fig. 29: Comparison in the muon flux at the emulsion between the measurement and prediction for the 250 kA horn operation. The band shows the uncertainty of the prediction.

Table 14: Comparison of the muon flux at the emulsion detector between the measurement and prediction. The fluxes are normalized to  $4 \times 10^{11}$  p.o.t.

	0 kA			250 kA		
	flux tracks /cm <sup>2</sup>	flux ratio (Data/MC)	fitted profile width (cm)	flux tracks /cm <sup>2</sup>	flux ratio (Data/MC)	fitted profile width (cm)
Data	$10892 \pm 126$	-	$122.4 \pm 6.5$	$40628 \pm 468$	-	$105.6 \pm 4.1$
T2K MC	9682	1.12	100.3	41833	0.971	98.7

prediction. This is because the phase space of secondary pions contributing to the muon flux at the emulsion is less constrained by the external data. This result demonstrates that our understanding of the muon, and hence neutrino, production is quite good for the 250 kA horn setting.



## 8. Conclusion

In this paper, we described the measurement of the beam direction by the muon monitor and the study of the muon yields with the emulsion detector. The systematic error of the beam direction measurement with the muon monitor was estimated to be 0.28 mrad and fulfills our requirement of  $< 0.3$  mrad. The muon beam direction has been stable, and controlled within 0.3 mrad for most of the span of beam operation and measured with good resolutions. As a consequence, we have controlled the neutrino beam direction well within 1.0 mrad and provided good quality beam data to be used as an input to the neutrino oscillation measurements. The muon monitor has also played in an important role in surveying the configuration of the beamline components. To confirm our understanding of muon beam and neutrino beam, the absolute muon flux was measured with the emulsion detector with a precision of 2%. It was then compared with prediction based on external hadron interaction data. As a result, we obtained good agreement between the data and prediction. This result confirms the validity of the beam control by the muon monitor and also demonstrates the validity of the T2K neutrino flux tuning based on the external hadron production data.

## Acknowledgment

We thank the J-PARC staff for superb accelerator performance and the CERN NA61 collaboration for providing valuable particle production data. We also would like to thank the J-PARC neutrino beam group for their putting great efforts to keep taking high quality beam data and the Nagoya University for helping us with the emulsion detector construction. We acknowledge the support of MEXT, Japan, and SNSF and Canton of Bern, Switzerland. Special thanks go to Nikhul Patel, who carefully reads this manuscript. In addition, authors have been further supported by funds from JSPS, Japan.

## References

- [1] K. Abe et al. (T2K collaboration), Nucl. Instrum. Meth., **A659**, 106–135 (2011).
- [2] K. Matsuoka et al., Nucl. Instrum. Meth., **A624**, 591–600, doi:10.1016/j.nima.2010.09.074 (2010).
- [3] A.K. Ichikawa, Nucl. Instrum. Meth., **A690**, 27–33 (2012).
- [4] K. Abe et al. (T2K collaboration), Nucl. Instrum. Meth., **A694**, 211–223 (2012).
- [5] S.J. Harris and C.E. Doust, Radiat. Res., **66**, 11 (1976).
- [6] H.J. Ziock et al., IEEE Trans. Nucl. Sci. NS-40, 344 (1993).
- [7] T. Higuchi et al., eConf C **0303241**, TUGT004, hep-ex/0305088 (2003).
- [8] A. Ferrari et al., CERN-2005-010 (2005).
- [9] K. Abe et al., Phys. Rev. D, **80**, 012001 (2013).
- [10] R. Brun, F. Carminati, and S. Giani, CERN-W5013 (1994).
- [11] C. Zeitnitz and T. A. Gabriel, In Proc. of International Conference on Calorimetry in High Energy Physics (1993).
- [12] M. Hartz et al., Nucl. Instrum. Meth., **A703**, 45–58 (2013).
- [13] T. Nakamura et al., Nucl. Instrum. Meth., **A556**, 80–86 (2006).
- [14] N. Armenise et al., Nucl. Instrum. Meth., **A551**, 261–270 (2005).
- [15] V. Tyukov et al., Nucl. Instrum. Meth., **A559**, 103–105 (2006).
- [16] N. Abgrall et al. (NA61/SHINE Collaboration), JINST, **9**, P06005 (2014).
- [17] N. Abgrall et al. (NA61/SHINE Collaboration), Phys. Rev. C, **84**, 034604 (2011).
- [18] N. Abgrall et al. (NA61/SHINE Collaboration), Phys. Rev. C, **85**, 035210 (2012).
- [19] T. Eichten et al., Nucl. Phys. B, **44**, 333 (1972).
- [20] J. V. Allaby et al., High-energy particle spectra from proton interactions at 19.2 GeV/c, Technical Report 70-12, CERN (1970).
- [21] I. Chemakin et al., Phys. Rev. C, **77**, 015209 (2008).
- [22] R.P. Feynman, Phys. Rev. Lett., **23**, 1415 (1969).
- [23] M. Bonesini et al., Eur. Phys. J. C, **20**, 13 (2001).
- [24] D. S. Barton et al., Phys. Rev. D, **27**, 2580 (1983).

[25] P. Skubic et al., Phys. Rev. D, **18**, 3115 (1978).